Department of Mechanical Engineering
Dynamics and Control section

Institute of Robotics and Mechatronics
Department of Analysis and Control of Advanced Robotic Systems

Experimental study of nonlinear normal modes in robotics: analysis and control strategies

Internship within the Master's Program Systems and Control

Cedric van Ruler (1395742)

External Supervisor:
MSc M.Keppler (DLR)
Prof. dr. ir. Alin Albu-Schäffer (DLR)

Internal Supervisor:
Prof. dr. ir. A.Saccon

Eindhoven, January 23, 2023

Abstract

Robots are used in a wide variety of tasks ranging from search and rescue, manufacturing and palletizing applications. In the last twenty years there has not only been interests in accurate robots but also compliantly actuated robots which resembles more the human dynamical capabilities. Research has shown that physical compliance is key to increase a robot's mechanical robustness and explosiveness, which allows to outperform the dynamics of stiff robots. Besides that, the energy storing capabilities promises more energy efficient cyclic motions. However, there exist still no general method to generate energy efficient motions for complex scenarios such as manipulation.
Normal modes are specific patterns of motion or vibration that a system can exhibit, and they are important for understanding the underlying dynamics of a system. Executing motions close to the normal modes of the system can potentially results in more efficient cyclic motions. While linear normal modes (LNMs) exactly characterize linear systems, this is not the case for nonlinear dynamical systems where a different framework is necessary to obtain nonlinear normal modes (NNMs). It is still unknown whether NNMs can be used to perform cyclic movements in a more energy efficient way on a real-life compliantly actuated system. Another research question is, what are the effects of various parameters on these NNMs such as change in stiffness settings and change in energy due to damping and friction. These questions will be investigated in this work.
First, NNMs will be identified and analysed which are interesting for particular hammering motions on the 4 DOF left arm system of the anthropomorphic compliantly actuated robot David using a nonlinear normal modes toolbox developed at the German Aerospace Center (DLR). Further, a new control strategy is developed named Energy Pumping (EP) Control to stabilize the modes by compensating for energy losses due to frictions or to switch to modes on different energy levels. Finally, this control algorithm is compared to Elastic Structure Preserving (ESP) Control in terms of performance and the effect of intentional impacts on the modes has been analysed.

Contents

Nomenclature

Groups, algebras, and sets

$\mathbb{R}$	The set of real numbers
$\mathfrak{M}$	Eigenmanifold
$\mathfrak{R}$	Generator

Roman symbols

t	Global time
q	joint variable
T	Kinetic field
V	Potential field
E	Energy

Greek symbols

Δx	Spring deflection
θ	Motor coordinates
σ	Stiffness preset

Subscripts and superscripts

$\dot{(\cdot)}$	First time derivative
$\ddot{(\cdot)}$	Second time derivative

Chapter 1

Introduction

This chapter serves as the introduction for this report. First, background information about the nonlinear normal modes (NNMs) framework are given. Then an overview of the David arm system is shown and the mechanism of the Variable Stiffness Joint (VSA) is briefly explained. The problem formulation and report structure will also be provided in this chapter.

1.1 Background on nonlinear normal modes

A normal mode (or mode) is a particular pattern of motion or vibration that a system can exhibit when it is perturbed from its equilibrium state. These patterns, or modes, are characterized by their frequency and shape, and are determined by the system's physical properties and constraints. Normal modes are used to analyze and predict the dynamic behavior of a system and can be used in the design and optimization of its performance. For linear systems the concept of (linear) normal modes is already widely used, consider the following linear system with n degrees of freedom (DOF)

$$M\ddot{q} + K(q - q_{eq}) = 0 \tag{1.1}$$

where $M \in \mathbb{R}^{n\times n}$ is the mass matrix, $K \in \mathbb{R}^{n\times n}$ is the stiffness matrix, $q \in \mathbb{R}^n$ is the displacement vector and $\ddot{q}$ is the acceleration vector. In this case a modal transformation can be performed which allows the decomposition of a coupled n-DOF system into n independent single-DOF systems, a superposition of the linear responses reconstructs the original response (as explained in [1]). However, this framework only holds for small oscillations for the linear approximation of a nonlinear system. Consider the nonlinear David arm link dynamics which can be described by the multi-body dynamics equation

$$M(q)\ddot{q} + C(q,\dot{q})\dot{q} + \frac{\partial V}{\partial q}(q,\sigma) = \tau \tag{1.2}$$

where $q \in \mathbb{R}^4$ are joint coordinates, $\dot{q}$ are the velocities, $\ddot{q}$ are the accelerations and the stiffness adjuster is indicated by σ. The inertia matrix $M(q) \in \mathbb{R}^{4\times 4}$ of the rigid links and $C(q,\dot{q})\dot{q} \in \mathbb{R}^{4\times 4}$ combines the Coriolis and centrifugal terms. The generalized external forces that are exhibited by the environment are represented by τ. Further, V which is the nonlinear part denotes the potential field induced by gravity and elastic terms. The total energy E of the system (1.2) is

$$E(q,\dot{q}) = \frac{1}{2}\dot{q}^T M(q)\dot{q} + V(q). \tag{1.3}$$

The nonlinear eigenmodes (neigenmodes [2]) toolbox developed at DLR uses the eigenmanifold theory which aims for extending eigenspaces outside of small oscillations to characterize families of large-amplitude nonlinear oscillations. An eigenmanifold $\mathfrak{M} \subset \mathbb{R}^{2n}$ is defined as a two-dimensional

invariant submanifold of the state space. The invariance is here defined with respect to the dynamics in Equation (1.2) and thus relevant for nonlinear oscillations. In this case, there are $n = 4$ distinct eigenmanifolds associated with an equilibrium q_{eq}, each one of them is tangent to a different linear eigenspace. The equilibrium position q_{eq} can be chosen by fixing the motor positions θ at a desired equilibrium. The direct extension of the eigenvectors are called generators $\mathfrak{R}$ which will be used as set of initial conditions with $\dot{q} = 0$. An eigenmanifold is a continuous set of periodic orbits (also known as eigenmodes or modes) that can be uniquely identified by their constant energy. For small energies, these orbits will resemble the ones predicted by the linear analysis. The neigenmodes toolbox produces the following results for a given system:

- All the generators, as a discrete set of points
- All the eigenmanifolds, as a discrete set of points
- Cycle period time of the eigenmodes.

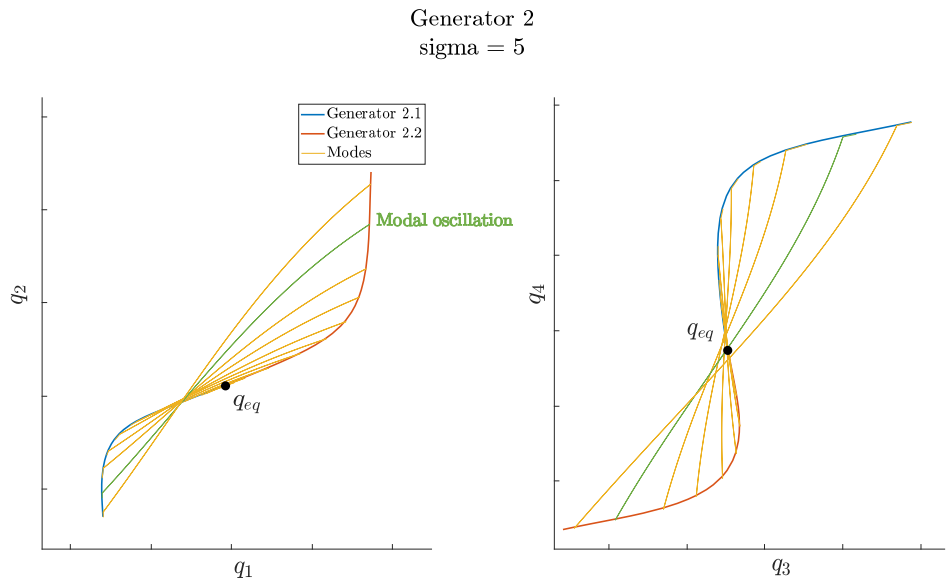

Figure 1.1: Projection of generator on the configuration space of the system. The generator for one specific group of modal oscillation is shown.

One example of the projection of a generator on the configuration space of the 4-DOF David arm system can be seen in Figure 1.1, in this case Generator 2 with stiffness preset $\sigma = 5°$ (stiffness preset is explained in Chapter 1.2). Herein one specific group of modal oscillation is shown of the system were the end points (with zero velocity) are forming the generator. The neigenmodes toolbox produces this generator as set of points, which are all starting points of modal oscillations (green line). Essentially, starting from a generator, the system will perform the corresponding modal oscillation back and forth forever if no torques are applied onto the system. The generator can be divided into two sub-generators separated by the system's equilibrium position, every mode is connected to both sub-generators at the end points, e.g., Generator 2.1 and 2.2 in Figure 1.1. Basically, this subdivision is splitting the generators in half and only one half is necessary to reconstruct the periodic orbits.

Note that at the time of writing this report the neigenmodes toolbox has not been published yet and no further details can be given.

1.2 David arm system

The theories in this work will be based on the anthropomorphic arm system of David which can be written in the form of (1.2). It consists of variable stiffness actuated joints which have energy storing capabilities. These passively compliant robots allow to outperform stiff robots in terms of robustness against collisions and impacts without severe damage. In case of collision the decoupling of drive and link, through to energy storage, results in lower peak torques in contrast to stiff robots which cannot store energy (for more details on the arm design see [3]). The following properties hold:

Property 1: The mass matrix $M(q)$ is symmetric and positive definite.

Property 2: The singular values of $M(q)$ are bounded above and bounded below away from zero, therefore $M^{-1}(q)$ exist and is bounded.

Property 3: Since $C(q,\dot{q})$ is bounded in q and linear in $\dot{q}$, C is bounded for bounded $\dot{q}$.

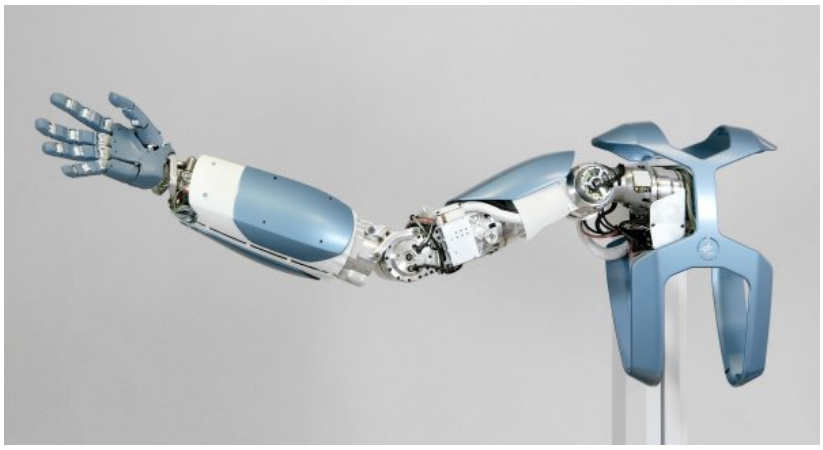

Figure 1.2: DLR Arm System. Source: [3]

The first four joints of the arm will be considered which consist of the DLR FLoating Spring Joints (FSJ) [4] (see Figure 1.3). The forearm and wrist joints are driven by Bidirectional Antagonistic Variable Stiffness (BAVS) joints which will not be included in this work. The joint positional limits can be seen in Table 1.1.

	Lowerbound [deg]	Upperbound [deg]
q_1	-86	136
q_2	0	171
q_3	-146	81
q_4	-31	141

Table 1.1: Joint limits

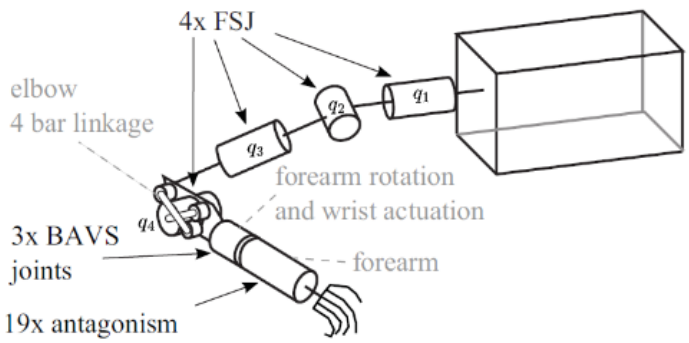

Figure 1.3: Location and name of the drive principles. Source: [3]

Floating Spring Joint (FSJ)

The first four arm joints, namely the elbow and the three shoulder joints, are implemented by Floating Spring Joints (FSJ) and will be considered during this work. The motor joints and links are connected via a variable nonlinear elastic element (see Figure 1.4a). The joint stiffness characteristics can be changed via the motor position σ. In Figure 1.4b is shown how different stiffness positions σ influence the joint stiffness characteristics. In this work σ is considered as a preset parameter and will not be changed when performing motions. The motor joint position θ (which is the reflected motor position after the gearboxes) will be used to hold the system in a desired equilibrium position. This parameter will also be determined prior executing any movements in the system.

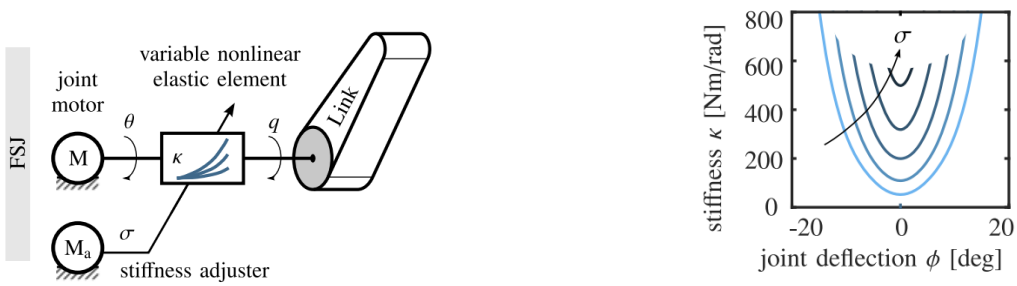

(a) Floating Spring Joint (FSJ)

(b) Joint stiffness characteristics for various stiffness adjuster positions

Figure 1.4: FSJ drive principle and joint stiffness characteristics for various stiffness adjuster positions $\sigma = \begin{bmatrix} 0 & 2.5 & 5 & 7.5 & 10 \end{bmatrix}^\circ$. Source: [5]

The maximum possible passive joint deflection $\varphi = \theta - q$ is decreasing with higher stiffness preset σ, this is due to saturation effects of the spring combined with the potential energy stored in the spring through the stiffness preset (can be seen in Figure 1.4b). The joint deflection bounds are determined by

$$q_{lowerbound} = \theta_0 - q_{max} \quad \text{and} \tag{1.4}$$

$$q_{upperbound} = \theta_0 + q_{max} \tag{1.5}$$

with the motor equilibrium θ_0 and the maximum link deflection q_{max}. During this work the joint deflection bounds are indicated by a grey dotted box on the configuration space of the system.

1.3 Problem statement

Often dynamical capabilities of systems are not yet sufficient for several tasks, for example in cyclic tasks (hammering) or highly dynamic tasks (throwing) actuators often can not provide enough energy during peak loads. Physical compliance also promises more energy efficient cyclic motions compared to stiff robots when using the system's normal modes. Using normal mode can potentially improves the performance of a system in these aspects. A normal mode (or mode) is a particular pattern of motion or vibration that a system can exhibit when it is perturbed from its equilibrium state. These patterns, or modes, are characterized by their frequency and shape, and are determined by the system's physical properties and constraints. Normal modes are used to analyze and predict the dynamic behavior of a system and can be used in the design and optimization of its performance. When initializing the system on a certain mode, the system's natural behaviour is following the mode and therefore the hypotheses is that when performing motions on or close to these modes it can lead to improvement benefits in performance (e.g. energy efficiency, accuracy or robustness) compared to non-modal control strategies on a real system. In the case of a linear system, linear normal modes can be obtained by performing a modal transformation which allows the decomposition of a coupled n-DOF system into n independent single-DOF systems, a superposition of the linear responses reconstructs the original response. However, for nonlinear systems (such as the David arm system in the form of (1.2)) these theories only apply for small oscillations for the linear approximation of a nonlinear system. Therefore, the nonlinear normal modes of the David arm system will be analysed by using the neigenmodes toolbox developed at DLR to numerically compute these Nonlinear Normal Modes for a given nonlinear system based upon the eigenmanifold theory.
The framework of NNMs assumes the system to be conservative. However, real systems are not conservative, meaning there is damping and friction acting on the dynamics of the system causing dissipation in energy. The research goal is to investigate how to generate NNMs on the David robot arm system and how to compensate for unavoidable energy dissipation due to friction to be able to stabilize a desired mode and asses if those friction compensated NNMs provide performance benefits (e.g. energy efficiency, accuracy or robustness) for cyclic motions compared to non-modal control strategies on a real setup, employing a hammering task as a prototype motion for the investigation. The David 4-DOF arm model will therefore be extended with a hammer model. Impacts are occurring when hitting the object after each hammering cycle which are also not included in the framework of NNMs, these impacts results in external forces applied on the dynamics of the system. Therefore, the effect of intentional impacts on NNMs are also investigated in this work.

1.4 Report structure

The previous section explained why using NNMs could be interesting to investigate for the purpose of improving a system's performance for cyclic motions. The remainder of this report is organized as follows, Chapter 2 describes the robot model kinematics which is used to compute the NNMs and an extension of this model with a hammer model is given. Interesting NNMs suitable for hammering tasks and an experimental analysis of the effects of link-side damping on NNMs which provide a basis for new control strategies to compensate for energy dissipation are shown in Chapter 3. To compensate for the unavoidable energy dissipation due to friction, a new energy based control strategy has been implemented to stabilize the NNMs, the performance of this energy based controller has been compared to Elastic Structure Preserving (ESP) control and the effect of intentional impacts on NNMs are analysed in Chapter 4. Conclusions and future work suggestions are presented in Chapter 5.

Chapter 2

Robot model

An Unified Robot Description Format (URDF), which is an XML format for representing the physical and visual properties of a robot (including e.g., its links and joints), will be used as input by the nonlinear eigenmodes toolbox to compute the generators and modes in Chapter 3. URDFs has become popular with the advent of the Robot Operating System (ROS), which is an open-source framework for building robotic applications. In Chapter 2.1, the robot model will be explained and how multiple robot links will be combined to reduce the URDF size to speed up the computation time of the neigenmodes toolbox. The neigenmodes toolbox computes the equations of motion using the URDF. However, the elastic potential function cannot be defined in the URDF. Therefore, the user must implement this potential function separately, the implementation of the elastic potential function is explained in Chapter 2.3. Also, the inertia of a hammer will be determined analytically and experimentally and integrated into the URDF of the arm system in Chapter 2.2, consequently two different URDFs are available to compute the NNMs.

2.1 David arm system URDF

URDFs of the David system can be generated using the David kinematics library from DLR. This library generates the desired URDF file for a specified set of sub-units of the David system (see Figure 2.2). In this case an URDF with the pedestal (P), torso (T), rightarm (Ar) and the righthand solid (Hs) has been created. Since computing the modes are computational intensive the solid hand was chosen. Only the first four links, R1-S1, R2-S2, R3-OA and R4-EK are defined as revolute in the URDF (see Figure 2.2), the others are fixed.

To reduce the computation time of the generators, the URDF file can be reduced by merging the fixed links R5-UA, R6-AB and R7-FL.
First, the position of the link's center of mass relative to its corresponding link-frame are given by ${}^{R5}\vec{r}_{cm_{R5}}$, ${}^{R6}\vec{r}_{cm_{R6}}$ and ${}^{R7}\vec{r}_{cm_{R7}}$. The mass of each link are m_{R5}, m_{R6} and m_{R7} which results in a total mass of

$$m_{R5,R6,R7} = m_{R5} + m_{R6} + m_{R7}. \tag{2.1}$$

The link's moments of inertia about its center of mass w.r.t. the link's frame of orientation are given by $J_{cm_{R5}}$, $J_{cm_{R6}}$ and $J_{cm_{R7}}$ (this can be found in Appendix A).
Further, all positions of the link's center of mass will be expressed relative to link-frame R_5 by

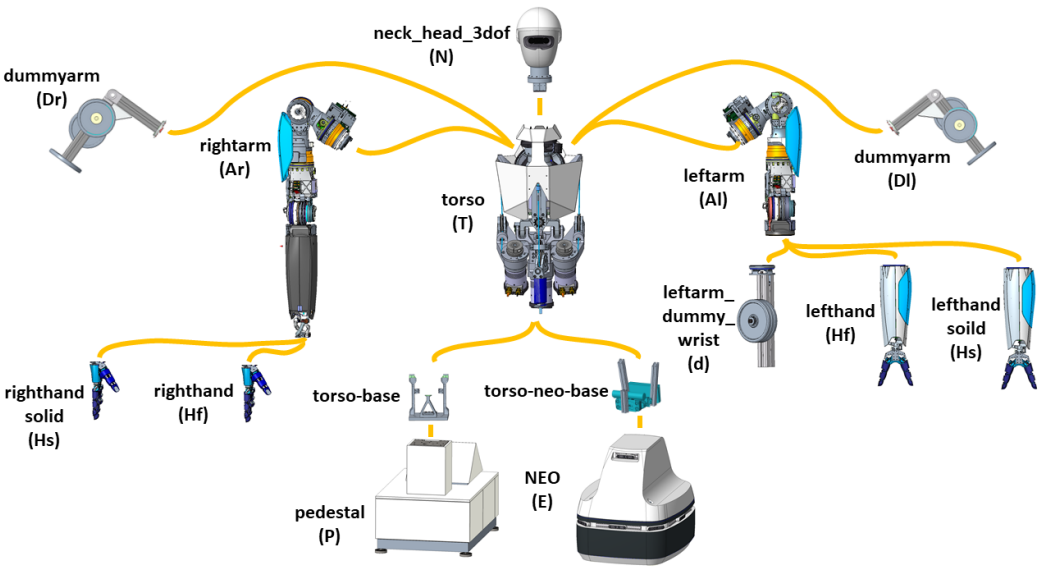

Figure 2.1: David sub-units to be selected for the David kinematics library. Source: [6]

applying the following rotation matrices

$$R_{R6} = R_y(\beta)R_x(\gamma) = \begin{bmatrix} \cos\beta & 0 & \sin\beta \\ 0 & 1 & 0 \\ -\sin\beta & 0 & \cos\beta \end{bmatrix} \begin{bmatrix} 1 & 0 & 0 \\ 0 & \cos\gamma & -\sin\gamma \\ 0 & \sin\gamma & \cos\gamma \end{bmatrix}, \tag{2.2}$$

$$R_{R7} = R_y(\beta) = \begin{bmatrix} \cos\beta & 0 & \sin\beta \\ 0 & 1 & 0 \\ -\sin\beta & 0 & \cos\beta \end{bmatrix} \tag{2.3}$$

where, $\beta = \gamma = -\frac{\pi}{2}$.
The positions of the link's center of mass relative to link R_5 are now defined by (see Figure 2.3):

$$^{R5}\vec{r}_{cm_{R6}} = R_{R6} \cdot {}^{R6}\vec{r}_{cm_{R6}}, \tag{2.4}$$

$$^{R5}\vec{r}_{cm_{R7}} = R_{R7} \cdot {}^{R7}\vec{r}_{cm_{R7}}. \tag{2.5}$$

The new center of mass of the three links relative to link R_5 (not indicated anymore) is defined by

$$\vec{r}_{cm_{R5,R6,R7}} = \frac{m_{R5} \cdot \vec{r}_{cm_{R5}} + m_{R6} \cdot \vec{r}_{cm_{R6}} + m_{R7} \cdot \vec{r}_{cm_{R7}}}{m_{R5} + m_{R6} + m_{R7}}. \tag{2.6}$$

Finally, the Huygens–Steiner theorem can be applied to combine all three inertia's by the following formula

$$J_{CM_{R5,R6,R7}} = \sum_{i=R5}^{R7} (J_{cm_i} + m_i(\vec{r}_i \cdot \vec{r}_i I - \vec{r}_i \vec{r}_i^T) \tag{2.7}$$

where, $\vec{r}_i = \vec{r}_{cm_i} - \vec{r}_{cm_{R5,R6,R7}}$.
The computational results can be found in Appendix A.

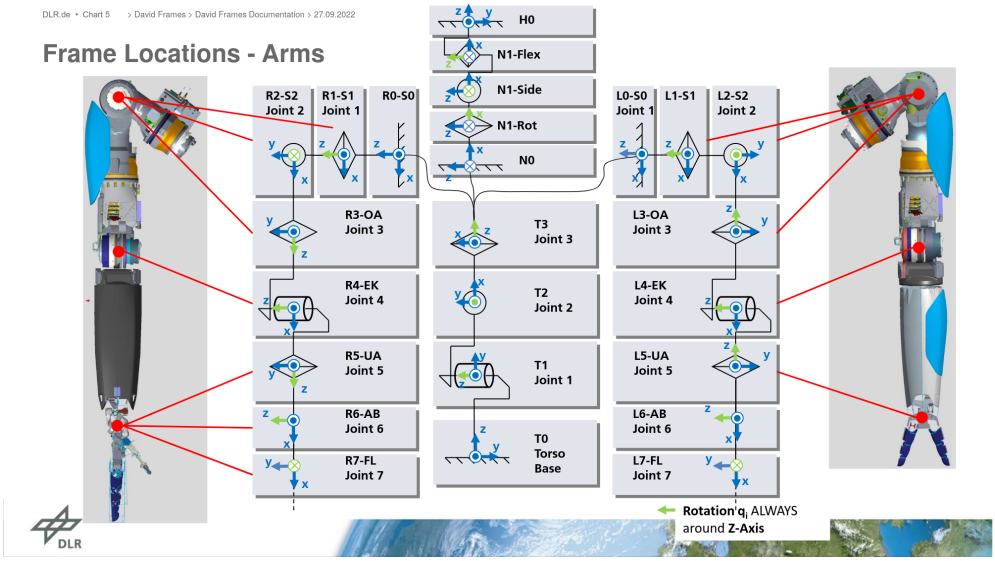

Figure 2.2: Frame Locations - Arms
Source: [6]

2.2 Hammer inertia model

The next step would be to add the inertia and mass of the hammer and calculate the new center of mass together with link five (calculated in the previous subsection). Upon completing this part, there are two URDF files at our disposal: one for the David arm model with a hammer model, and one for the David arm model without a hammer model. The moment of inertia of the hammer is calculated experimentally and analytically.

2.2.1 Experiment using period of oscillation

For the experiment the moment of inertia is computed by using the period of oscillation of the hammer. The period of oscillation is the time it takes for an object to complete one cycle of motion, in this case swinging back and forth. For the experiment the period time of the hammer is measured around the xx and zz axis as depicted in Figure 2.4, J_{yy} and off-diagonal terms are not critical for hammering motions. Around the center of rotation there is a small mass with an unknown inertia, to reduce the effects of this mass a rope is attached between the hammer and the center of rotation. The rope is assumed to be massless. Pictures of the real experimental setup can be found in Appendix B. The mass moment of inertia is calculated by using the period of oscillations defined as

$$T = 2\pi\sqrt{\frac{J_o}{mgd}} \tag{2.8}$$

where T is the period time which will be measured, $m = 0.64kg$ is the mass of the hammer, $g = 9.81ms^2$ is the gravity constant, $d = d_1 + 0.268$ is the distance from the rotation axis to the center of mass and I is the moment of inertia around I_o. The moment of inertia around the center of mass is calculated with

$$J_{cm} = J_o - md^2. \tag{2.9}$$

For the axis xx and zz three experiments have been performed as shown in Table 2.1, with an average

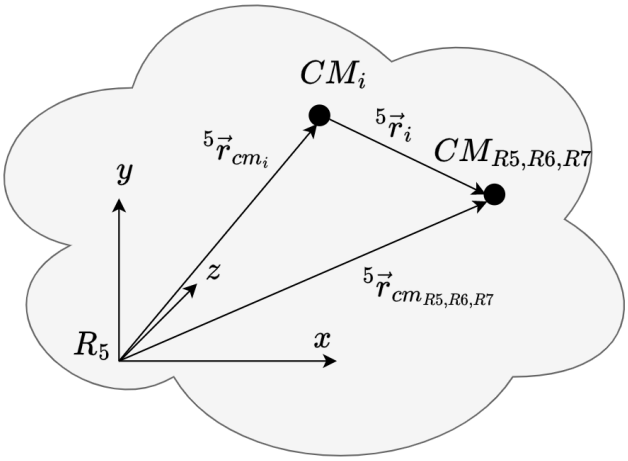

Figure 2.3: Position from link's center of mass to combined center of mass

inertia around the center of mass of

$$J_{cm,measured} = \begin{bmatrix} 0.0042 & & \\ & J_{yy} & \\ & & 0.0036 \end{bmatrix} \text{kg}\,\text{m}^2. \tag{2.10}$$

	Experiment 1		Experiment 2		Experiment 3	
	xx	*zz*	*xx*	*zz*	*xx*	*zz*
d_1 [m]	0.394	0.360	0.405	0.484	0.480	0.473
T [s]	1.655	1.604	1.651	1.747	1.742	1.735
J_o [kg m^2]	0.2884	0.2570	0.2917	0.3650	0.3610	0.3547
J_{cm} [kg m^2]	0.0079	0.0045	0.0019	0.0031	0.0029	0.0033

Table 2.1: Experimental results hammer inertia

2.2.2 SolidWorks modeling of hammer inertia

For the analytical computation the hammer is approximated by using SolidWorks with three shapes, ellipse, rectangular parallelepiped and triangle (see Appendix C for the dimensions). The total mass of the hammer is measured to be 0.640 kg and based on the assumption that the hammer head mass must be 0.20 kg, 0.30 kg, 0.50 kg or 0.80 kg, the head mass is 0.50 kg and the handle must therefore weigh 0.14 kg. Based on this information the following inertia matrix is computed around the center of mass of the hammer

$$J_{cm,solidworks} = \begin{bmatrix} 0.0038 & 6.64 \cdot 10^{-5} & 0 \\ 6.64 \cdot 10^{-5} & 0.00043 & 0 \\ 0 & 0 & 0.0041 \end{bmatrix} \text{kg}\,\text{m}^2. \tag{2.11}$$

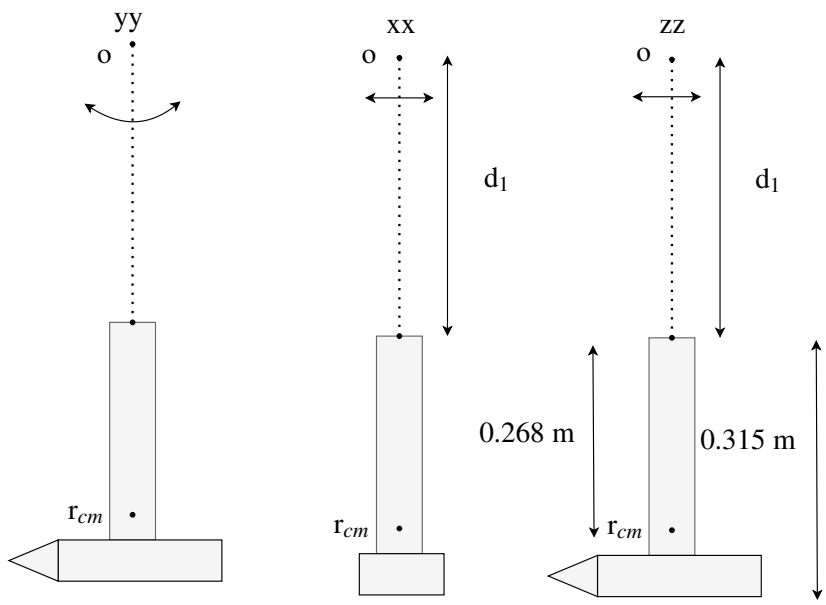

Figure 2.4: Hammer experiment configuration

2.2.3 URDF with hammer

The inertia matrix of the experimental and analytical results are relatively close to each other. The final inertia matrix used will be the average between those two

$$J_{cm_{hammer}} = \begin{bmatrix} 0.0040 & 6.64 \cdot 10^{-5} & 0 \\ 6.64 \cdot 10^{-5} & 0.00043 & 0 \\ 0 & 0 & 0.0039 \end{bmatrix} \text{kg}\,\text{m}^2. \tag{2.12}$$

From now on $\vec{r}_{cm_{R5}} = \vec{r}_{cm_{R5,R6,R7}}$, $m_{R5} = m_{R5,R6,R7}$ and $J_{cm_{R5}} = J_{cm_{R5,R6,R7}}$ (see Equation (2.6), (2.1) and (2.7)).
For the new URDF, the hammer inertia will be combined with $R5$. The new center of mass becomes

$$\vec{r}_{cm_{R5,hammer}} = \frac{m_{R5} \cdot \vec{r}_{cm_{R5}} + m_{hammer} \cdot \vec{r}_{cm_{hammer}}}{m_{R5} + m_{hammer}} \tag{2.13}$$

where, $\vec{r}_{cm_{hammer}} = \begin{bmatrix} 0.08 & 0.22 & 0 \end{bmatrix}^T$ m is measured by hand on the real hardware. The vector from the center of mass of R5 to the new center of mass of R5 and the hammer combined defined as

$$\vec{r}_{R5} = \vec{r}_{cm_{R5,hammer}} - \vec{r}_{cm_{R5}}. \tag{2.14}$$

Further the vector from the center of mass of the hammer to the new center of mass of R5 and the hammer combined is

$$\vec{r}_{hammer} = \vec{r}_{cm_{R5,hammer}} - \vec{r}_{cm_{hammer}}. \tag{2.15}$$

The combined inertia around the center of mass will be (see Appendix C for the solutions)

$$\begin{aligned} J_{cm_{R5,hammer}} =& J_{cm_{hammer}} + m_{hammer}(\vec{r}_{hammer} \cdot \vec{r}_{hammer}\, I - \vec{r}_{hammer}\vec{r}^T_{hammer}) + \ldots \\ & J_{CM_{R5}} + m_{R5}(\vec{r}_{R5} \cdot \vec{r}_{R5} I - \vec{r}_{R5}\vec{r}^T_{R5}). \end{aligned} \tag{2.16}$$

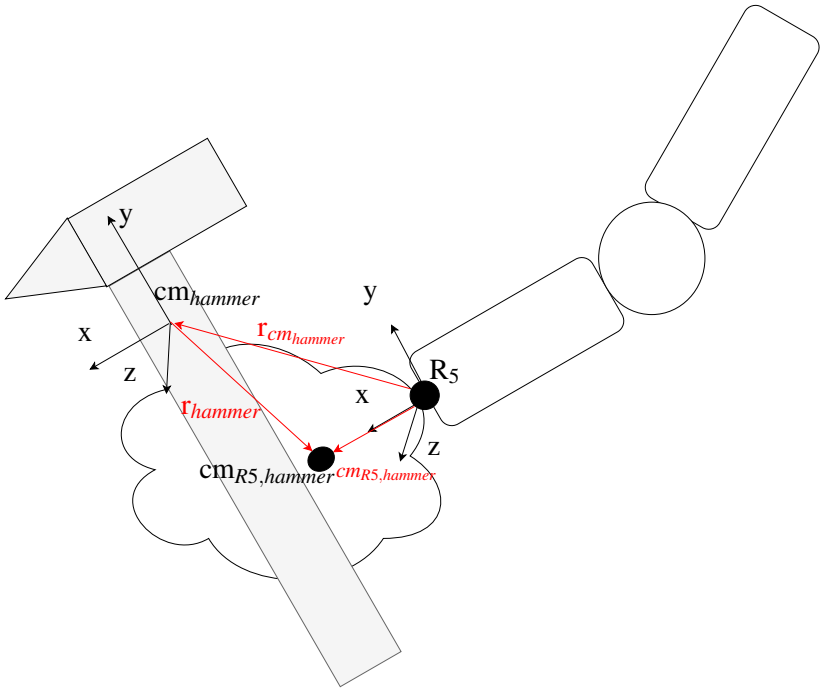

Figure 2.5: New center of mass $cm_{R5,hammer}$ for Link R_5 and the hammer combined.

2.3 Potential function

Besides the URDF, the neigenmodes toolbox also requires the potential function since this cannot be obtained from the URDF. The spring energy is described by [4]

$$E_{store}(\phi) = \frac{1}{2}R(\Delta x^2(\phi) - x_0^2), \tag{2.17}$$

with spring constant R, spring deflection Δx and pretension x_0.
The spring force results in

$$F_{spring}(\varphi) = \sqrt{2R(E_{store} + E(x_0))}. \tag{2.18}$$

The derivative of the cam disk in dependency of φ is defined as

$$\frac{\partial x}{\partial \varphi} = \frac{\tau_{cam}(\varphi)}{F_{spring}(\varphi)}, \tag{2.19}$$

with the torque characteristics of the cam disk τ_{cam} and the passive joint deflection φ. For more details about the spring potential see section E of [4].
The differential equation can be numerically integrated along φ to derive the cam profile. In the simulation and on the hardware a lookup table is used for the cam profile since no analytic solution could be found. However, the toolbox requires an analytic convex expression for the potential function. Therefore, the cam profile lookup table is approximated by the eight order polynomial with the following structure

$$f(x) = p_1x^8 + p_2x^7 + p_3x^6 + p_4x^5 + p_5x^4 + p_6x^3 + p_7x^2 + p_8x + p_9, \tag{2.20}$$

with $p_1 = -52.41$, $p_2 = -180.9$, $p_3 = -188.1$, $p_4 = 0.2258$, $p_5 = 128.2$, $p_6 = 91.97$, $p_7 = 27.31$, $p_8 = 3.577$ and $p_9 = 1.194$.
The variance of the polynomial fit is 0.99996 m^2 and Root Mean Square Error of 0.015083 m. The passive joint deflection vs the torque characteristic curve can be found in Appendix D for both the lookup table and the fitted polynomial function.

Chapter 3

Nonlinear Normal Modes on David

In Chapter 3.1, motor positions will be suggested which give rise to interesting NNMs with as goal to perform hammering motions. These motions are performed by assuming no energy dissipation or external forces acting on the system. In Chapter 3.2, the NNMs computed by the neigenmodes toolbox are verified with the David arm simulation. In Chapter 3.3, the effects of link-side damping will also be investigated which causes energy dissipation. Note that the URDF model which has been used does not include the hammer model.

3.1 Hammering modes

Based on the discussed work in Chapter 2, namely the creation of the URDF model of the David arm system and the implementation of the elastic potential function, the NNMs and generators can be computed for the David arm system using the neigenmodes toolbox. To compute the NNMs, two different preset parameters need to be chosen in the elastic potential function namely, the joint stiffness preset σ and the motor equilibrium position θ. The output of the toolbox results in four eigenmanifolds and four generators, the generators is used as a set of initial conditions for the system with $\dot{q} = 0$ and the eigenmanifold is used to have an interpretation of the corresponding motion. There does not exist a systematic method to determine the equilibrium position and stiffness preset for a desired modal trajectory yet. Therefore, the desired generators will be found based on trial and error using visualisations of the David arm system and the projection of the eigenmanifold on the joint space of the system. In first instance, the ideal motion for a hammering task would be a perfect vertical movement of the hand palm from a frontal perspective with a frequency of around 2 Hz, the problem with higher frequent modes is that it will probably be harder to excite on the real system compared to lower frequent modes. However, when such a mode cannot be found the primary focus of analysing the motion is the hand palm motion at the bottom position when the joints are close to zero velocity to be vertical or close to vertical, as this is relevant to the hammering task of striking a nail. Two interesting hammering modal candidates are shown in this section.

Candidate 1: elbow driven hammering motion

To have an idea how a hammering motion looks like in joint space, joint data on the hardware is collected of a desired hammering motion trajectory, which is indicated by the green line in Figure 3.1. The first step is to choose a desired motor equilibrium position θ, this is determined by computing the joint coordinates during maximum velocity of the measured hammering data trajectory. The reason for that is that the modes are at maximum velocity around the equilibrium position (in this specific case), which coincides with the midpoint of the motion of one modal trajectory. The joint

equilibrium positions are

$$q_{eq} = \begin{bmatrix} -26 & 9 & 7.5 & 79 \end{bmatrix}^{\circ}.$$

Next, the stiffness preset σ needs to be chosen, all four joints are set to the same stiffness values. The mode shapes of the second generator with stiffness preset $\sigma = 5^{\circ}$ were the most corresponding to the measured hammering data, see Figure 3.1. Visualisation snapshots of the simulation (purple line) can be seen in Figure E.1 located in Appendix E. Unfortunately, modes at higher energy levels which are located outside of the maximum deflection bounds are closer to the green line but cannot be used on the real setup. The modal frequency is around $f = 5$ Hz for low energy levels (inside the grey box). Changing the stiffness preset has effects on the period time, see Figure 3.2b. Generally, lower stiffness setting σ results in a lower frequency, also modes corresponding to lower energy levels yields lower frequent modes (see Figure 3.2b). Experiments on the hardware shows that releasing the system from initial conditions close to this generator results in a different movement then expected. Observed is that the elbow joint damps out almost immediately and only a sideways motion driven by the shoulder is visible consisting of a lower frequency of around $f = 2$ Hz. The theoretical mode is mainly driven by movements of the fourth joint corresponding to the elbow joint causing probably high frequent modes. Observed is that the shoulder takes over the motion, which consists of a lower natural frequency. This showed that probably lower frequent modes which are mainly driven by q_1 (first shoulder joint) are easier to excite then higher frequent modes which are mainly driven by q_4 (elbow joint) on the real setup. Therefore, the second modal candidate is shown which consists of a motion mainly driven by the first shoulder joint (with a frequency of around $f = 2$ Hz) since the end goal is to perform these modes on the real setup.

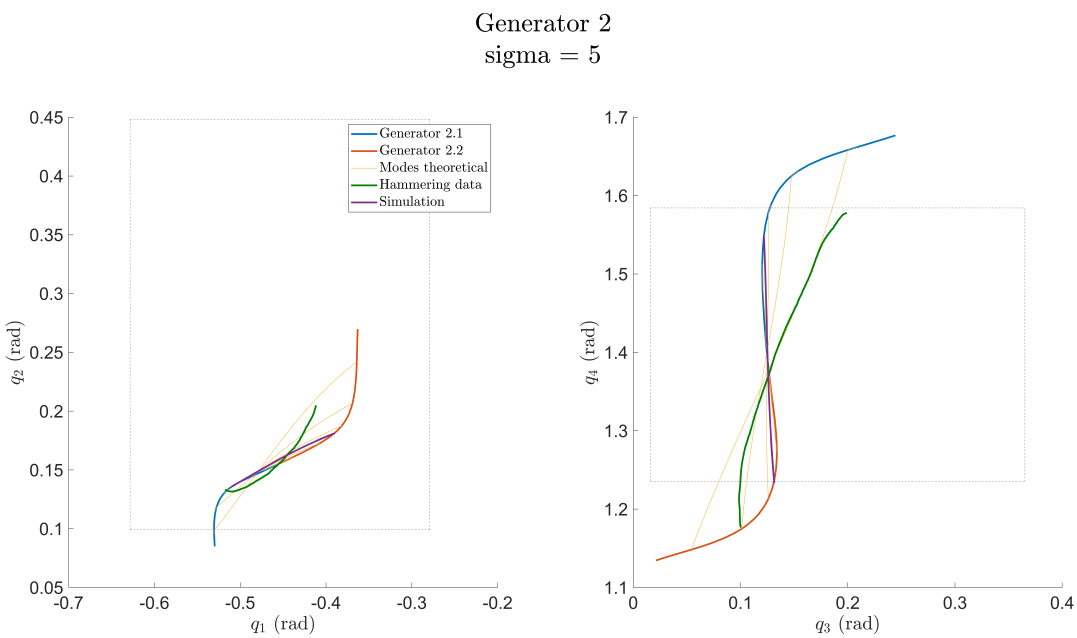

Figure 3.1: Generator 2 for equilibrium position of $q_{eq} = \begin{bmatrix} -26 & 9 & 7.5 & 79 \end{bmatrix}^{\circ}$ with measured hammering data (green curve).

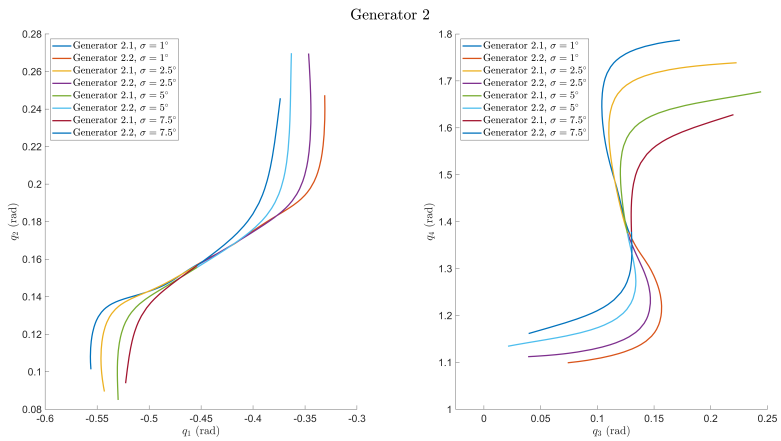

(a) Generator 2

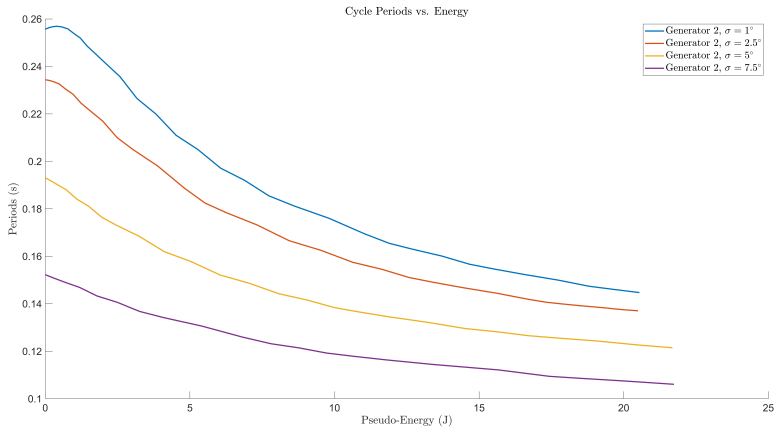

(b) Cycle periods of modes

Figure 3.2: Effect of various stiffness settings applied to all joints ranging for $\sigma = \begin{bmatrix}1 & 2.5 & 5 & 7.5\end{bmatrix}°$, Generator 2 is shown for various stiffness settings in Figure 3.2a and the modal period time can be seen for various energy levels in Figure 3.2b.

Candidate 2: shoulder driven hammering motion

The second modal candidate uses less elbow motion but more movements from the first shoulder joint q_1. In this case the corresponding frequency is around $f = 2$ Hz which was desired. The found generator can be seen in Figure 3.3. Visualisation snapshots of the simulation (purple line) can be seen in Figure E.2 located in Appendix E. The mechanical design of the first shoulder joint is slightly inwards rotated (direction to the body) around the x axis (Figure 2.2), the hammering motion is therefore also rotated inwards and is not a vertical path anymore from a frontal perspective. The hammering data is not shown in this figure since this motion is not located close to the new manifold. The equilibrium corresponding to this new candidate results in

$$q_{eq} = \begin{bmatrix}-30 & 10 & -10 & 100\end{bmatrix}°.$$

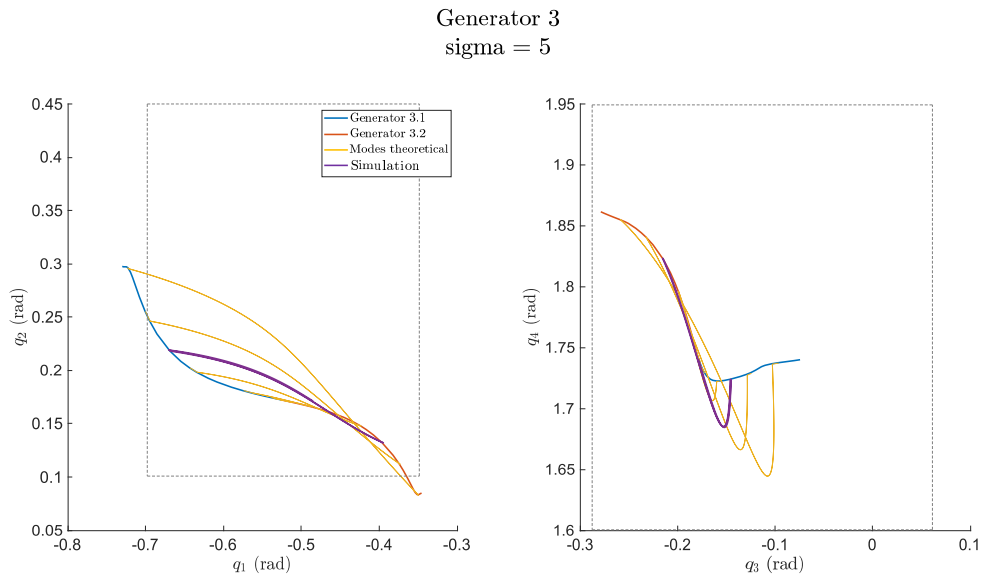

Figure 3.3: Generator 3 for equilibrium position of $q_{eq} = \begin{bmatrix} -30 & 10 & -10 & 100 \end{bmatrix}^\circ$.

3.2 Comparing generators with simulation

Simulations are performed to validate the existence of the modes in the simulation environment. In this case candidate 1 is used with an initial condition of

$$\vec{q}_0 = \begin{bmatrix} -0.530 \\ 0.088 \\ 0.235 \\ 1.673 \end{bmatrix} \text{ rad.}$$

As shown in Figure 3.4, there is a small error when ending on Generator 2.2, this error occurs due to numerical issues. After one modal trajectory the errors are still very small

$$\vec{q}_{error} = \begin{bmatrix} 0.0007 \\ 0.0003 \\ 0.0009 \\ 0.0010 \end{bmatrix} \text{ rad.}$$

This error is the difference in angular position between the simulation and the generated mode at zero velocity. However, the error increases when simulating for longer time and the simulation will eventually diverge from the desired mode to infinity but this will not be an issue due to the implemented control algorithms explained later in this work. On the real system damping is involved which will cause energy dissipation, the effects of damping will be discussed in Chapter 3.3.

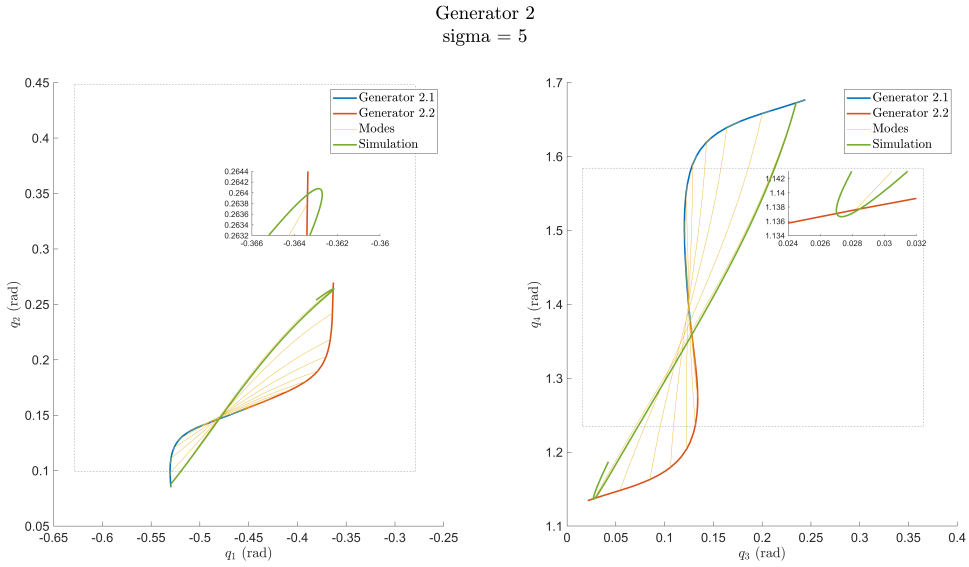

Figure 3.4: Simulated vs theoretical mode

3.3 Effects of damping on nonlinear normal modes

The generators are computed with the assumption there is no link-side damping acting on the system. However on the real system there will be damping present. In this section the effects of link-side damping acting on the system is experimentally investigated. On real systems positive damping does not exist, but nevertheless it would be interesting to investigate it with regard to possible control implementations. Positive damping results in energy injection (see Figure 3.5a) and negative damping results in energy dissipation (see Figure 3.5b). Note that the simulated motions are moving along with the generators which is an interesting property for control purposes. The energy level cannot be influenced when initializing the system from the equilibrium since the initial velocity is and remain zero. The link-side damping has exponential effects on the energy levels which can be seen in Appendix F.

3.4 Conclusion

This chapter showed two different groups of manifolds which could be interesting for the purpose of hammering tasks. Candidate 1: elbow driven hammering motion, closely resembles the desired vertical hammering motion (shown as the green line in Figure 3.1), but the modal frequency was approximately twice as high as desired. Candidate 2: shoulder driven hammering motion, this motion uses more of a combination between the first shoulder joint and the elbow joint. This motion was not perfectly vertical from a frontal perspective but consists of the desired frequency of around $f = 2$ Hz, which is probably more realistic on the real setup. Therefore, candidate 1 will serve as prototype motion for the development of control strategies to stabilize a desired mode by compensating for energy dissipation in Chapter 4. Adjusting the stiffness preset of each joint individually may result in more suitable modes for a hammering task. However, this increases the number of potential configurations significantly. Manually finding a desired NNMs is time consuming not only due to the computational time, but also because it is affected by various variables such as equilibrium position and joint stiffness settings. Additionally, the modes of each generator must be visualized to determine if they are suitable for the desired purpose. As the number of degrees of freedom in

a system increases, the number of potential configurations grows exponentially. Therefore, possible future research includes finding ways to reverse this process, such that a desired one can be given as input and the parameters that result in NNMs close to the desired mode can be identified.

It is well-known that damping acting on a system results in energy dissipation. However, it was not clear how damping was effecting the NNMs of a system since the NNMs are computed by assuming conservative systems. In Chapter 3.3, an experimental investigation was conducted which showed that link-side damping in a system not only causes the system to converge to the equilibrium position by dissipating energy, but also preserves the modal shape as the system moves along the generators and return to the equilibrium position. The inverse also holds, when configuring the system with positive damping (causing energy injection), the system is moving along the generators to higher energy levels. Even tough link-side damping cannot be controlled directly through software, it means that modes can potentially be stabilized by regulating energy levels of the system. In Chapter 4, an energy based control algorithm is implemented based on this concept.

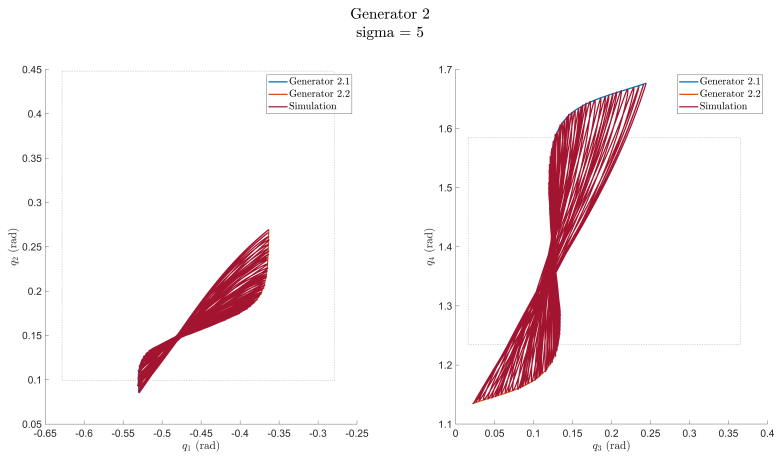

(a) Simulated modes for the energy dissipation case with damping factor of 0.1. The system is initialized at an energy level of 20J (located towards the end of the generator) and is converging to the equilibrium position.

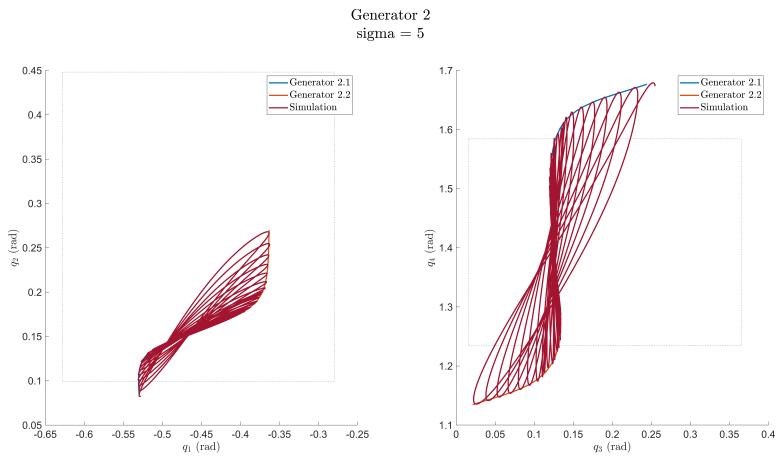

(b) Simulated modes for the energy injection case with damping factor of -0.1. The system is initialized at an energy level of 0.06J close to the equilibrium position.

Figure 3.5: Effects of link-side damping in eigenspace. For higher damping factors the motion will move faster along the generators resulting in less dense motion curves. The system also moves faster along the generators at higher energy levels compared to lower energy levels which can also be observed in the figures.

Chapter 4

Stabilization of nonlinear normal modes

Based on the results in Chapter 3.3, regulating energy levels can potentially be used to stabilize and control NNMs. In Chapter 4.1.1, a controller has been implemented based on link-side damping control which in practice cannot be directly implemented since link-side damping is a characteristic of the physical properties of the system. However, it would still be interesting to validate this energy based method, as this could lead to the development of energy based control strategies that can be implemented on the real system. Energy Pumping (EP) control, a energy based control strategy to stabilize NNMs which is realizable on the real setup is explained in Chapter 4.1.2. In Chapter 4.2, the performance of Energy Pumping control is compared to that of Elastic Structure Preserving (ESP) control, which is a control strategy implemented on the David robotic arm developed at DLR. The goal of ESP control is to maintain the link-side inertial properties and the elastic characteristics of the original plant dynamics. Finally, intentional impacts are analysed on the NNMs in Chapter 4.3.

4.1 Energy regulating

In this section an energy regulating control strategy is explained which can be used to stabilize the desired modes. Modal candidate 2 will be used to demonstrate the developed control algorithm since these modes are more realistic to achieve on the real setup as explained in the previous chapter.

4.1.1 Link-Side Damping Control

As shown in Chapter 3.3 link-side damping can be used to regulate energy levels while staying on the generators. This is useful for modal stabilisation to able to stay in a desired mode but also for switching to other modes. Even though link side damping cannot be changed directly on the real system since it is a characteristic of the physical property of the real system, it is still meaningful to investigate whether energy based approaches can work to stabilize NNMs as a foundation of other control strategies. The following function is used to determine the link-side damping factor d to regulate energy levels (or see Figure 4.1)

$$d = K \cdot tanh(2 \cdot E_{error}) \tag{4.1}$$

where scaling factor $K = 0.2$ and $E_{error} = E - E_{desired}$.
The total energy is defined as

$$E = T + V_{grav} + V_{elast} - V_{eq}$$

where T is the kinetic energy, V_{grav} is the gravitational energy, V_{elast} is the elastic energy and V_{eq} is the energy in the equilibrium.

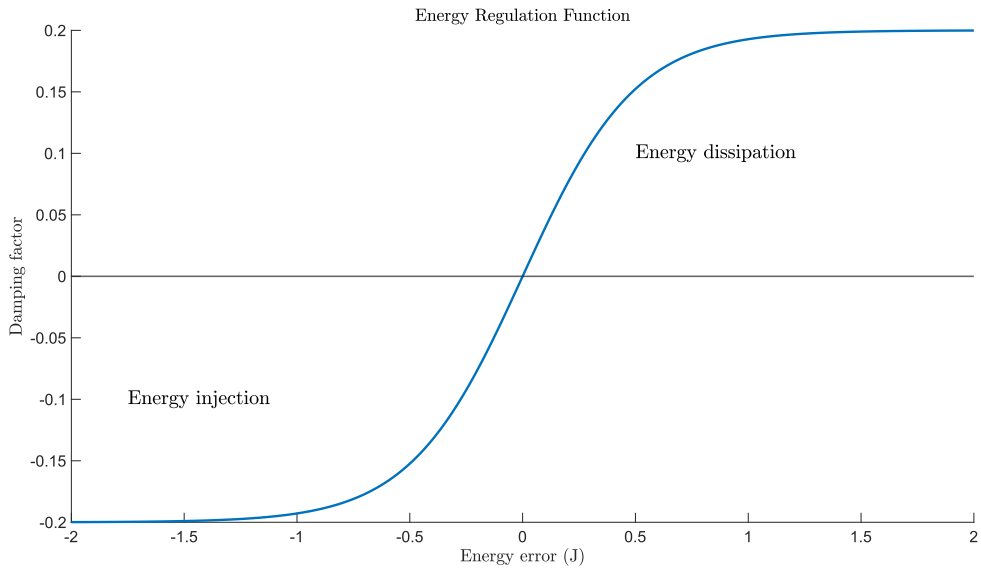

Figure 4.1: Energy regulating function

On the real system, the arm must begin from its equilibrium position, but there is no initial velocity and therefore energy levels cannot be changed from this position. ESP Control [5] is used to first increase energy levels by going from the equilibrium position to a desired position on the generator (indicated by the star symbol in Figure 4.2). Then a switch is enabled where the motor positions are set back to the equilibrium position by using a simple PD controller (with the same gains as on the real system, P=8000 and D=100) and the energy regulating algorithm will be enabled to stabilize the desired mode. This principle can be seen in Figure 4.2 and 4.3, q_0 indicates the goal position of the ESP controller and also the starting position of the energy regulating controller.

There is a oscillating steady-state error present of approximately 0.15 J. That the system is converging to the desired energy level does not necessary mean that the system is converging to the desired mode. The system could converge to other limit cycles with the same energy levels instead, therefore it is crucial to initialize the system close enough to the desired mode in this example the required error was $|q_{error,ss}| < 8 \cdot 10^{-4}$ rad. An observation is that for higher energy levels there is more margin for this initial condition error. Note that this method has also been successfully validated to switch between modes of different energy levels. In Chapter 4.1.2, another energy based control strategy is proposed that is designed for implementation on actual systems.

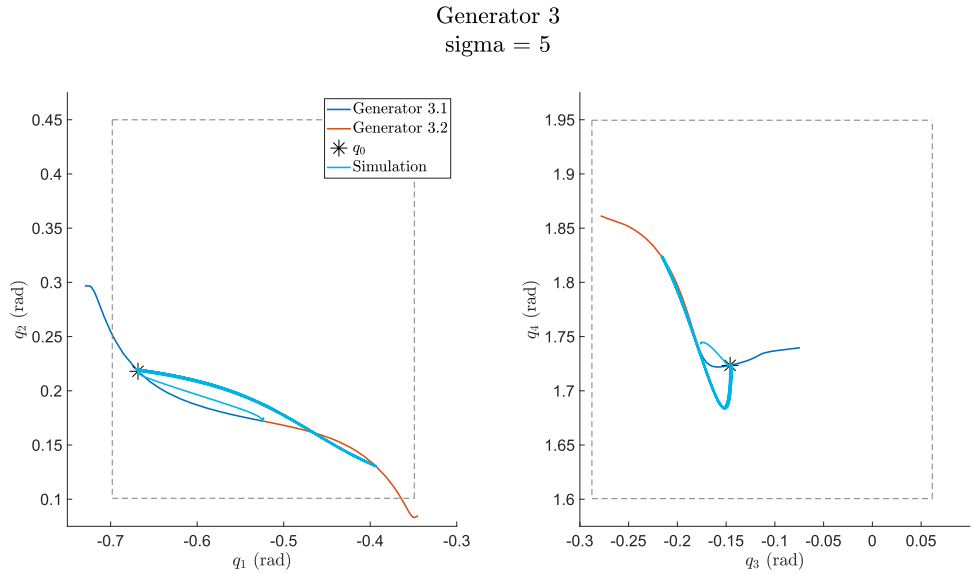

Figure 4.2: The system is initialized at the equilibrium position, using ESP control to go from the equilibrium to the star position (indicated by $*$) on the generator, switching motor position back to the equilibrium position (using PD control) and enabling link-side damping control. After releasing the system from the star position, the desired mode is stabilized. Note that the simulation time is $t = 5$ s and only the link positions are shown in the figure.

4.1.2 Energy Pumping (EP) Control

The energy based approach in Chapter 4.1.1 shows that using energy based approaches to control NNMs are promising. However, the previous approach cannot be implemented on the real system since the link side damping cannot be changed directly. Therefore a different approach to control energy levels is discussed in this section. This approach is based on injecting energy using change in motor positions. Consider the total energy H of a single elastic joint

$$H = S_\theta + S_q \tag{4.2}$$

where the motor side energy S_θ and link side energy S_q are defined as

$$S_\theta = \frac{1}{2} B\dot{\theta}^2 \quad \text{and} \tag{4.3}$$

$$S_q = \frac{1}{2}(M\dot{q}^2 + K(\theta - q)) \tag{4.4}$$

with, $q \in \mathbb{R}$ and $\theta \in \mathbb{R}$ represent the link and motor coordinates, respectively. $M \in \mathbb{R}$ is the inertia matrix of the rigid links, $B \in \mathbb{R}$ is the diagonal matrix of the actuator inertias reflected through the respective gearboxes. The spring energy with stiffness parameter k is chosen to be allocated on the link side.
The equations of motion on the motor- and link-side are given by

$$B\ddot{\theta} + K(\theta - q) = u \quad \text{and} \tag{4.5}$$

$$M\ddot{q} = K(\theta - q) \tag{4.6}$$

with the control input u. The change of energy on the link side follows as

$$\dot{S}_q = M\ddot{q}\dot{q} + K(\theta - q)(\dot{\theta} - \dot{q})) \tag{4.7}$$

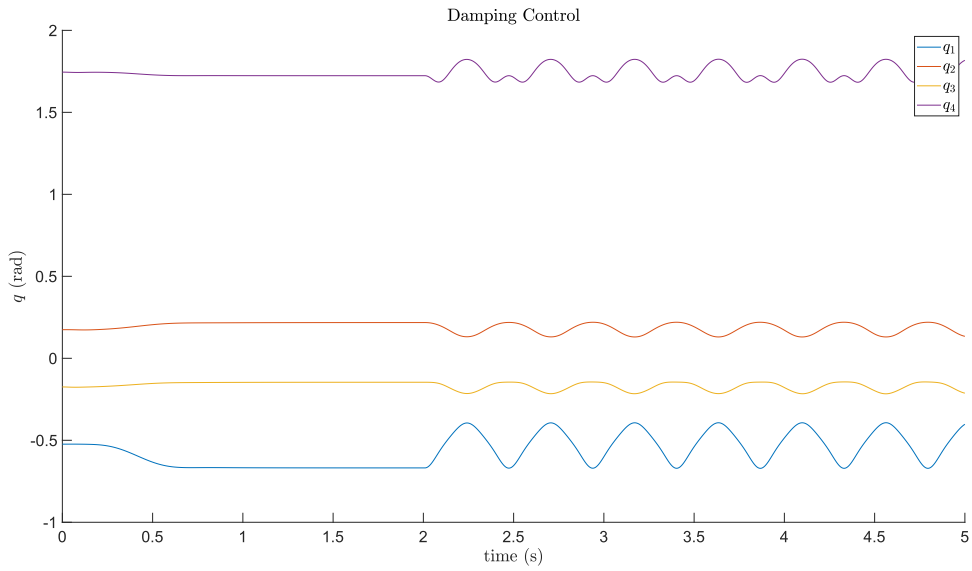

Figure 4.3: Joint positions over time

Substituting Equation (4.6) and the torque $\psi = K(\theta - q)$ yields

$$\dot{S}_q = \dot{q}\psi + \psi(\dot{\theta} - \dot{q}) \tag{4.8}$$
$$= \psi\dot{\theta}. \tag{4.9}$$

Note that $\dot{S}_\theta = -\psi\dot{\theta}$, by using the fact that $\dot{H} = 0$.
Equation (4.9) shows that energy will be injected to the system if both the torque ψ and the motor velocity $\dot{\theta}$ have the same signs. Energy will be dissipated when they have different signs. This principle can also be extended to the full dynamics of David, for reference see the passivity analysis in section V of [5].
This theory will be used to inject energy during maximum link velocity by moving the motors. This also means that the motors are not fixed at the equilibrium θ_0 anymore but the new desired motor coordinates θ_d are now defined as

$$\theta_d = \theta_0 + \Delta\theta \tag{4.10}$$

where θ_0 is the equilibrium position and $\Delta\theta$ is the variable motor offset which will be used to inject energy which is

$$\Delta\theta = \varepsilon \cdot \Delta q \cdot tanh(2 \cdot E_{error}) \tag{4.11}$$

with a scaling factor ε, the difference in maximum joint deflection of the mode Δq and the energy regulation function as variable scaling (see Figure 4.1).

4.2 Elastic Structure Preserving (ESP) Control

In this section, a modal trajectory will be given to the ESP controller [5] which is a control strategy implemented on the David robotic arm system and developed at DLR. The goal of ESP control is to maintain the link-side inertial properties and the elastic characteristics of the original plant dynamics. The desired trajectory is created by simulating the system for one period on a desired position on the generator, in this case a mode of approximately 3 J. Higher order derivatives (until fourth order) are computed from the measured position vector, these derivatives are required as feedforward terms for the ESP controller. One period can be repeated to create a longer trajectory signal. Note that due to numerical simulation errors, the end position of the periodic signal is not exactly the same as the starting position, this will cause small cyclical jumps when extending this signal. The steady error of the ESP trajectory control is $-0.02 < q_{error,ss} < 0.02$ rad.
The steady state trajectory of both control methods are shown in Figure 4.4. The positional error over time could not be compared to each other since the Energy Pumping Control uses energy as reference. Therefore, the Euclidean norm $\|q_e\|$ is calculated between the theoretical mode and the simulation as

$$\|q_e\| = \sqrt{\sum_{i=1}^{n}(q_i - qd_i)^2} \tag{4.12}$$

where the link coordinates are indicated by $q_n \in \mathbb{R}^{n\times 4}$ and the theoretical modal coordinates is $qd_n \in \mathbb{R}^{n\times 4}$, with n the length of the mode. Resulting in a Euclidean norm of

$$\|q_{e,EP}\| = 0.1838 \text{ rad} \quad \text{and} \tag{4.13}$$

$$\|q_{e,ESP}\| = 0.0294 \text{ rad} \tag{4.14}$$

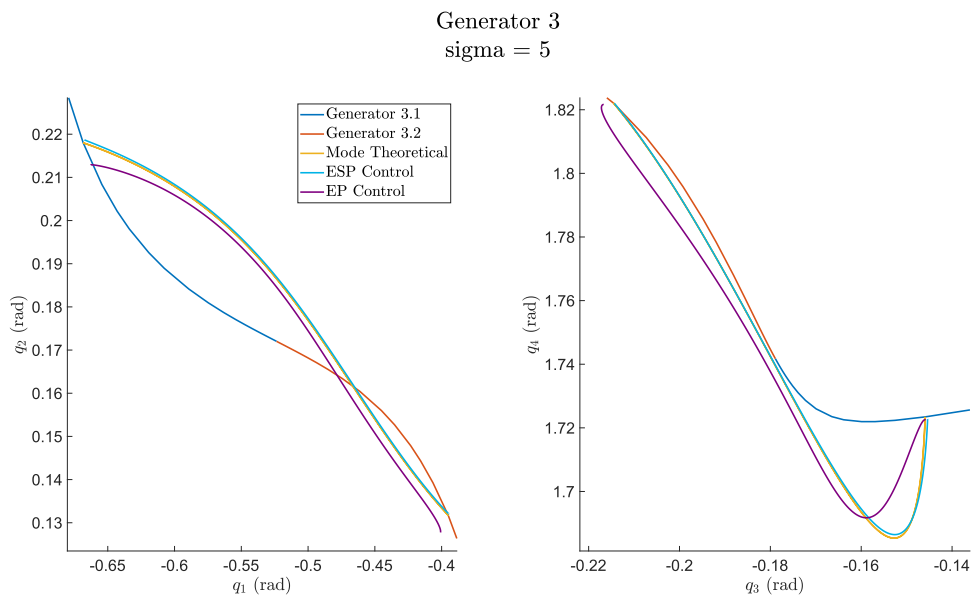

Figure 4.4: One modal trajectory in the steady state of ESP Control and EP Control

The variance for a random variable vector A made up of N observations is computed by

$$Var = \frac{1}{N-1}\sum_{i=1}^{N}|A_i - \mu|^2 \tag{4.15}$$

where μ is the mean of A,

$$\mu = \frac{1}{N}\sum_{i=1}^{N} A_i. \tag{4.16}$$

The variance of the x and y positions of the hand palm (TCP) at zero velocity results in

$$Var(x,y)_{EP} = \begin{bmatrix}0.9272 & 0.5438\end{bmatrix} \cdot 10^{-6}\,\mathrm{m}^2 \quad \text{and} \tag{4.17}$$

$$Var(x,y)_{ESP} = \begin{bmatrix}0.9251 & 0.4236\end{bmatrix} \cdot 10^{-12}\,\mathrm{m}^2 \tag{4.18}$$

In terms of accuracy and consistency ESP Control outperforms EP Control for this specific mode as shown above.
However, in terms of mechanical power the EP Controller shows to use less energy in the steady state as shown below

$$W_{EP} = \frac{1}{5}\int_{t=5}^{t=10} |u \cdot \dot{\theta}| = 2.93 \cdot 10^3\,\mathrm{W\,s} \quad \text{and} \tag{4.19}$$

$$W_{ESP} = \frac{1}{5}\int_{t=5}^{t=10} |u \cdot \dot{\theta}| = 4.75 \cdot 10^3\,\mathrm{W\,s} \tag{4.20}$$

where $u \in \mathbb{R}^4$ is the control torque input and $\dot{\theta} \in \mathbb{R}^4$ is the motor velocity. In this case the EP Controller is 1.6 times more efficient in terms of mechanical power. However, this depends strongly on the applied link- and motor-side frictions in the model. Increasing friction reduces the energy efficiency of the EP controller compared to the ESP controller. In the following example, the energy efficiency only improves factor 1.2 when doubling the motor-side friction D to

$$D = \begin{bmatrix} 2 & 0 & 0 & 0 \\ 0 & 2 & 0 & 0 \\ 0 & 0 & 2 & 0 \\ 0 & 0 & 0 & 2 \end{bmatrix} \tag{4.21}$$

and doubling the link-side friction K_d to

$$K_d = \begin{bmatrix} 0.2 & 0 & 0 & 0 \\ 0 & 0.2 & 0 & 0 \\ 0 & 0 & 0.2 & 0 \\ 0 & 0 & 0 & 0.2 \end{bmatrix}. \tag{4.22}$$

The relative performance of the EP and ESP controllers in terms of accuracy, variance and energy efficiency depends on various factors and requires further investigation. Factors such as the energy level of the NNM, control parameters, and the shape of the NNM can impact control performance. Besides that, both controllers utilize the NNM framework, meaning that both could benefit from its use. Therefore, it might be possible that both strategies perform better than control strategies that do not incorporate the system's NNM for similar motion patterns.

4.3 Effects of impacts on nonlinear normal modes

In this section the effects of impacts on the modes will be analysed in simulation. In this part modal candidate 1 will be used since this represents a more vertical hammering motion. The effects of impacts which lead to external counter forces applied in the direction of the mode will be investigated in this section. Only impact forces in the vertical z direction are considered as shown in Figure 4.5. The height at the moment of impact is z^* which is the vertical distance from the world frame to the moment of impact. The impact is modelled as a linear spring damper system resulting in an external force $F_{external,z}$ and is defined by

$$m\ddot{x} = -k(z - z^*) - d(\dot{z} - \dot{z}^*) \quad if \quad z < z^* \tag{4.23}$$

where $K = 6000$ is the stiffness coefficient and $d = 2000$ is the damping coefficient of the plateau. If $z \geq z^*$, no external forces are applied. Consequently, the four external joint torques $\tau_{ext} \in \mathbb{R}^4$ can be computed by

$$\tau_{ext} = J^T F_{ext} \tag{4.24}$$

where $J \in \mathbb{R}^{4x6}$ is the Jacobian converting the external forces on the TCP to joint torques and $F_{ext} = \begin{bmatrix} 0 & 0 & F_{ext,z} & 0 & 0 & 0 \end{bmatrix}^T$.

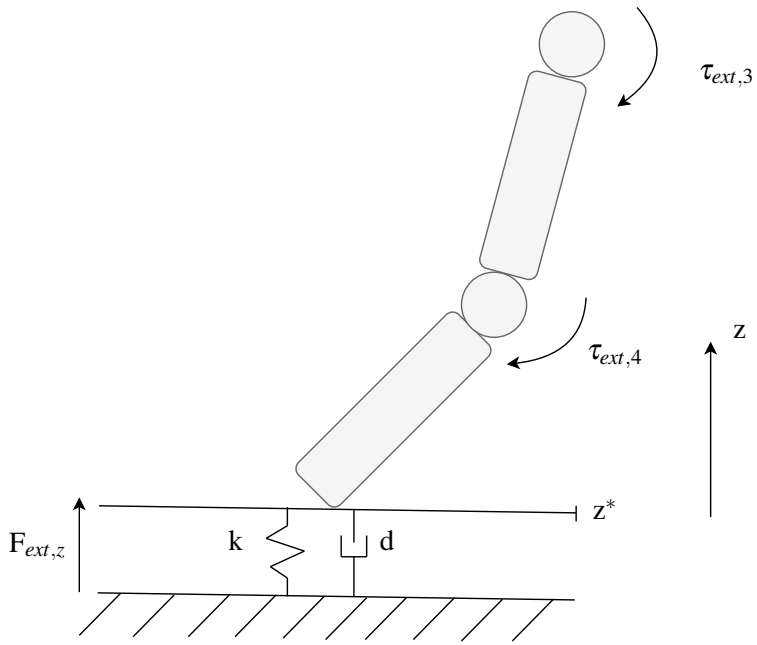

Figure 4.5: Impact model on David. Note that the system consist of four external joint torques but only two are shown in the figure.

The impact location depends on the hammering strategy. When the objective is to perform a single massive hit it is ideal to have the impact at maximum velocity. However when the goal is to have repetitive hammering motions it is desired to have impact locations close to the generator, otherwise too much kinetic energy is lost during the impact which can cause the destabilization of modes. It is crucial to find the correct trade-off, but this is subject to future work.
Without impacts the hand palm reaches a distance of around $z = -0.385$ m with respect to the first joint q_1. In this case the table height is chosen to be $z^* = -0.375$ m. That means the hand palm reaches the object about 1 cm before reaching its natural zero velocity point.
An observation is that the impacts do have effect on the phase of the modes and also causes an amplitude reduction as shown in Figure 4.6.

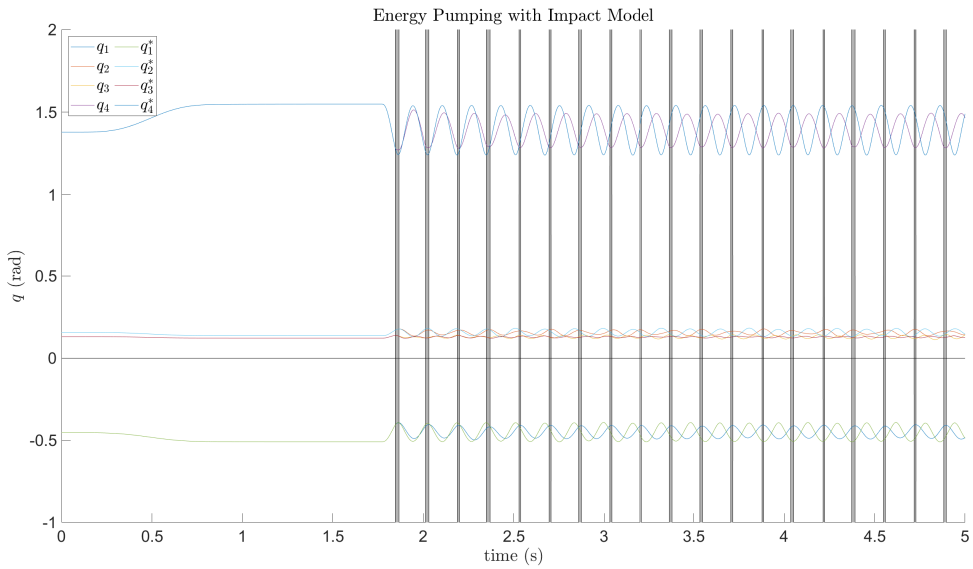

Figure 4.6: Joint position with q are the position from the original simulation and q^* are the positions with the applied impact model. The grey bars indicate the moments where the impact model is applied.

The shape of the motion does not change much, as shown in Figure 4.7. However, the error in energy has been increased by factor 10, from 0.2 J prior to 2 J after implementation of the impact model.

The most important aspect for hammering applications is the variance of the hand palm at zero velocity. A big variance results in inconsistency when it comes to hitting the nail. In Figure 4.9, the effects of impacts on the variance of the palm locations is shown. In this case, the impacts results in a increase of variance of nearly factor 15, which is from $Var(x,y) = \begin{bmatrix} 0.3969 & 0.4793 \end{bmatrix} \cdot 10^{-6}$ m^2 to $Var(x,y) = \begin{bmatrix} 0.1261 & 0.1764 \end{bmatrix} \cdot 10^{-5}$ m^2. The data points in Figure 4.9 are the x and y locations of the hand palm at the moment of crossing the table z^* in the falling direction. The variance can be reduced by implementing an iterative learning algorithm. In this method a force vector will be applied on each data point (in Figure 4.9) in the direction to the desired hand palm location. However, this method requires future investigation and will not be discussed in this work.

External forces caused by impacts have effects on the performed motion. As shown in Figure 4.6, there is a shift in amplitude and phase present compared to the original executed motion without the applied impact forces. This is observed under the condition the modes are disturbed at moments of low kinetic energy is the system.

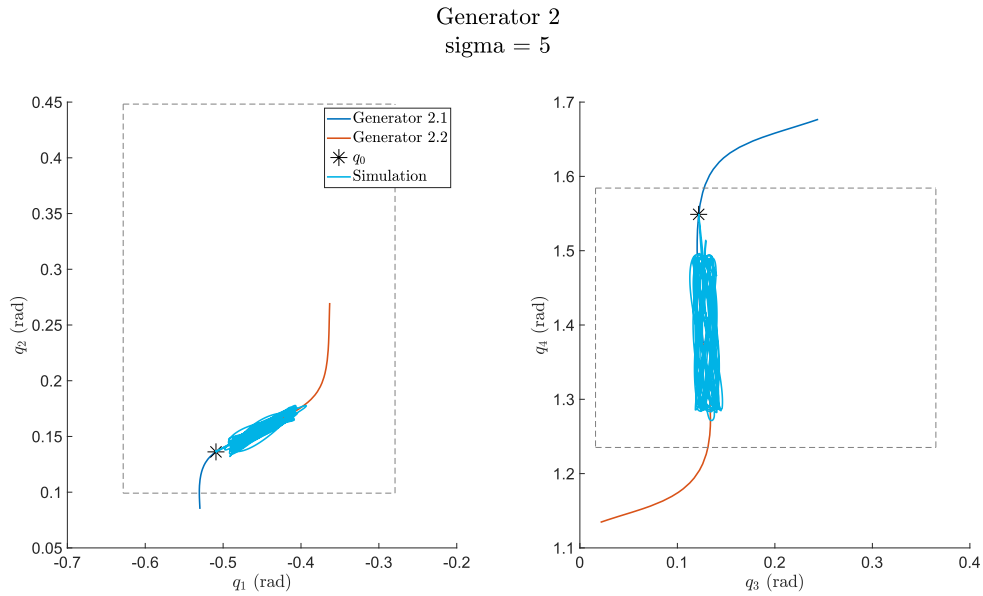

Figure 4.7: Motion with simulated impacts

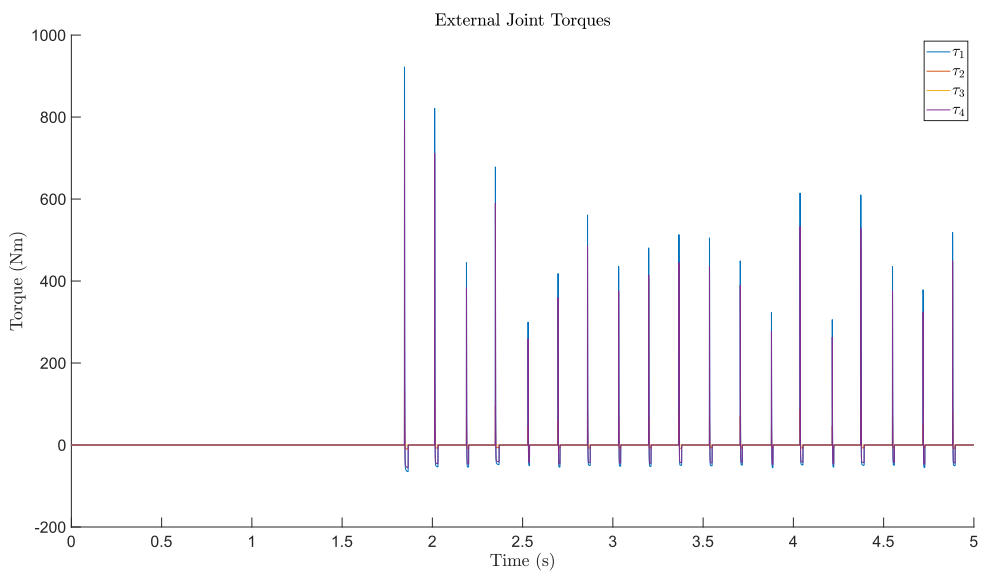

Figure 4.8: The external applied torque on each link resulting from the impact model

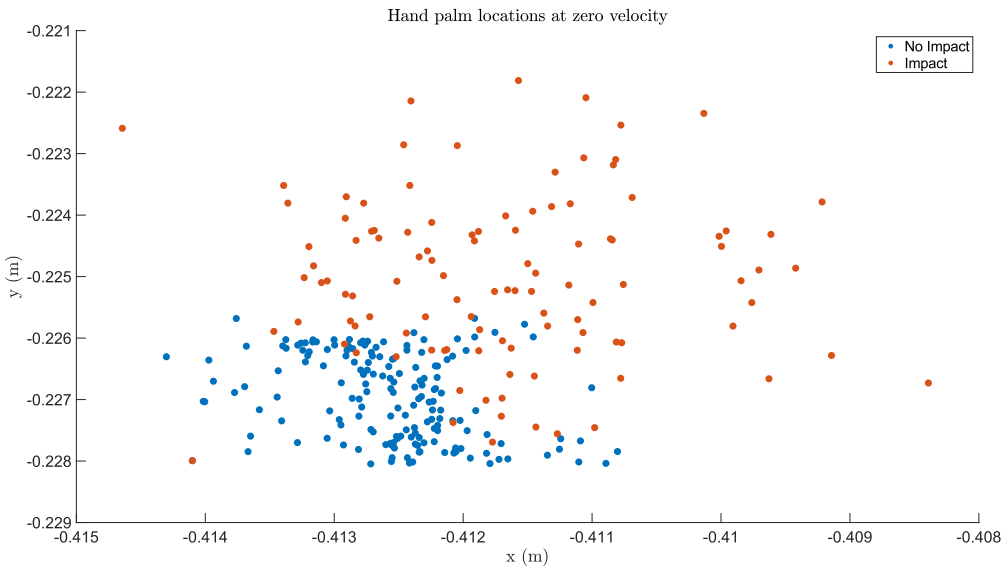

Figure 4.9: The palm locations at zero velocity, note that this simulation has been executed for 30 seconds to collect more data points

Chapter 5

Conclusions and future work

5.1 Conclusions

Throughout this report, experimental research is performed regarding the analysis and control of nonlinear normal modes applied in simulation on the David arm system. The research goal was to investigate how to generate Nonlinear Normal Modes (NNMs) on the David robot arm system and how to compensate for unavoidable energy dissipation due to friction to be able to stabilize a desired NNM and asses if those friction compensated NNMs provide performance benefits (e.g. energy efficiency, accuracy or robustness) for cyclic motions compared to non-modal control strategies on a real setup, employing a hammering task as prototype motion. Prior to this work, it was only possible to generate NNMs for an arbitrary mechanical system using the nonlinear eigenmodes toolbox. A objective of this study was the ability to generate NNMs for the specific 4-DOF David arm system, which is presented in Chapter 2. Further, two different generators and their corresponding NNMs which are useful for hammering motions are presented in Chapter 3.1. The NNMs shown in this study are still not ideal for the purpose of hammering applications on the real setup due to the non-vertical motion path or unwanted high modal frequency. It is possible that better NNMs for hammering tasks could be obtained by experimenting with different stiffness settings for each link individually. Also, a useful property is discovered during this work namely, the system stays on the generator for increasing and decreasing energy levels (caused by friction for example) after initializing the system on its generator. Energy Pumping (EP) control has been developed in this work using this property for the purpose of modal stabilization to compensate for unavoidable energy compensation in Chapter 4.1.2, which was another objective of this work. Subsequently, EP control has been compared in terms of performance with the Elastic Structure Preserving (ESP) control algorithm developed at DLR. No final statement can be drawn regarding performance in terms of energy efficiency, robustness or accuracy when comparing the energy pumping control with ESP control since not enough different generators are investigated and many parameters such as motor-side friction, link-side friction, energy level of the NNM have effects on its performance and requires further investigation. Also, tuning of the control parameters for the energy pumping control can have a significant impact on the performance. For the specific mode and parameter settings treated in Chapter 4.2, the ESP controller shows to be around 6 times more accurate in terms of distance to the desired mode during the steady state. This example also showed that the energy pumping control strategy was however 1.6 times more energy efficient in terms of mechanical power but showed that the efficiency decreases when increasing the motor and link-side friction. Finally, the effect of impacts has been experimentally analysed on the modes when using energy pumping control. In this case modal candidate 1 is used to investigate the effects for a vertical motion. The results showed that the inconsistency in the hand position at zero velocity (close to the moment of hitting the object) increases with nearly factor 15 for these specific parameter settings.

5.2 Future work

- **Finding NNMs more efficiently**
  Manually finding a desired NNMs is time consuming not only due to the computational time, but also because it is affected by various variables such as equilibrium position and joint stiffness settings. Additionally, the modes of each generator must be visualized to determine if they are suitable for the desired purpose. As the number of degrees of freedom in a system increases, the number of potential configurations grows exponentially. Therefore, possible future research includes finding ways to reverse this process, such that a desired NNM can be given as input and the parameters corresponding to this mode can be identified.

- **ESP with damping control**
  Chapter 4.1.1 showed that link-side damping control can be used to stabilize the modes by regulating energy levels. The problem with this method was that this parameter cannot be influenced directly using software. However, it would be interesting to investigate whether a hybrid between ESP control and damping control would work and how the performance will be in comparison with the other control strategies treated in this work. The idea is to regulate energy levels as explained in Chapter 4.1.1 by changing the damping parameter of the ESP controller. The desired trajectory of the ESP controller should be fixed at the equilibrium position of the system.

- **Impact analysis**
  Impact analysis has been performed for a specific two dimensional case. Future work includes extending the impact model to three dimensions and implementing a more accurate (nonlinear) impact model. Also, an investigation is needed to determine the ideal impact location on the mode by considering the trade-off between the lost of kinetic energy and the applied force on the object and to perform tests on the real hardware.

- **Iterative learning**
  It is recommended to implement an iterative learning algorithm to reduce the variance in terms of position when hitting the nail, especially when impacts are present. This can be implemented by applying a 2D force vector from the hitting location to the desired location (the nail).

- **Hardware implementation**
  Another step would be to implement the energy pumping algorithm on the real hardware and to analyse performance benefits compared to non-modal control strategies. Possibly this algorithm can also be improved by finding more efficient moments to inject energy into the system.

References

[1] S. Graham Kelly, "Mechanical Vibrations: Theory and Applications," in SI. 2012, pp. 533–588.

[2] F. Bjelonic, A. Sachtler, Y. Wotte, and D. Santina, *nEigenmodes!* Institute of Robotics and Mechatronics, Department of Analysis and Control of Advanced Robotic Systems, User manual nonlinear eigenmodes toolbox, Confidential document, 2021.

[3] M. Grebenstein *et al.*, "The DLR hand arm system," in *Proceedings - IEEE International Conference on Robotics and Automation*, 2011, pp. 3175–3182.

[4] S. Wolf, O. Eiberger, and G. Hirzinger, "The DLR FSJ: Energy based design of a variable stiffness joint," in *Proceedings - IEEE International Conference on Robotics and Automation*, 2011, pp. 5082–5089.

[5] M. Keppler, D. Lakatos, C. Ott, and A. Albu-Schaffer, "Elastic Structure Preserving (ESP) Control for Compliantly Actuated Robots," *IEEE Transactions on Robotics*, vol. 34, no. 2, pp. 317–335, Apr. 2018.

[6] Wolf Sebastian, Meyer Lukas, and Keller Sebastian, "David frames, Definition of coordinate frames and kinematic representation," Tech. Rep., Institute of Robotics and Mechatronics, Department of Analysis and Control of Advanced Robotic Systems.

Appendix A

Computational results of combining URDF links

The position of the link's center of mass relative to the link-frame R is defined by

$$
{}^{R5}\vec{r}_{cm_{R5}} = \begin{bmatrix} -0.00012808984 \\ 0.00030413187 \\ -0.17975399 \end{bmatrix} \text{m}
$$

$$
{}^{R6}\vec{r}_{cm_{R6}} = \begin{bmatrix} -0.01182179 \\ -0.0075132531 \\ 0.0079153582 \end{bmatrix} \text{m}
$$

$$
{}^{R7}\vec{r}_{cm_{R7}} = \begin{bmatrix} 0.10073161 \\ -0.0039917088 \\ -5.3873306 \cdot 10^{-5} \end{bmatrix} \text{m}.
$$

The mass of each link is, $m_{R5} = 4.744586$ kg, $m_{R6} = 0.11244899$ kg and $m_{R7} = 0.59139005$ kg. The new mass is the additions of the link's masses $m_{R5,R6,R7} = m_{R5} + m_{R6} + m_{R7} = 5.4484$ kg. The link's moments of inertia about the link's center of mass are given by

$$
J_{cm_{R5}} = \begin{bmatrix} 0.029653953 & -9.1947929 \cdot 10^{-6} & 1.551325 \cdot 10^{-5} \\ -9.1947929 \cdot 10^{-6} & 0.031286393 & 1.9468694 \cdot 10^{-5} \\ 1.551325 \cdot 10^{-5} & 1.9468694 \cdot 10^{-5} & 0.0075527898 \end{bmatrix} \text{kg}\,\text{m}^2
$$

$$
J_{cm_{R6}} = \begin{bmatrix} 7.3059504 \cdot 10^{-5} & 4.2102609 \cdot 10^{-7} & 1.9274652 \cdot 10^{-5} \\ -4.2102609 \cdot 10^{-7} & 5.8250807 \cdot 10^{-5} & -2.3749 \cdot 10^{-6} \\ 1.9274652 \cdot 10^{-5} & -2.3749 \cdot 10^{-6} & 7.6727465 \cdot 10^{-5} \end{bmatrix} \text{kg}\,\text{m}^2
$$

$$
J_{cm_{R7}} = \begin{bmatrix} 0.00070075841 & -9.8945275 \cdot 10^{-5} & -0.00019656949 \\ -9.8945275 \cdot 10^{-5} & 0.0019745327 & -0.00014518088 \\ -0.00019656949 & -0.00014518088 & 0.0016121161 \end{bmatrix} \text{kg}\,\text{m}^2.
$$

The inertia matrix around the center of mass of the combined links is

$$
CM_{R5,R6,R7} = \begin{bmatrix} 0.0533822995885104 & -7.46435603696223 \cdot 10^{-5} & 0.000425665159600031 \\ -7.46435603696223 \cdot 10^{-5} & 0.0562655656155791 & -0.000595565950015009 \\ 0.000425665159600031 & -0.000595565950015009 & 0.00931217486198841 \end{bmatrix} \text{kg}\,\text{m}^2.
$$

Appendix B

Hammer experiment setup

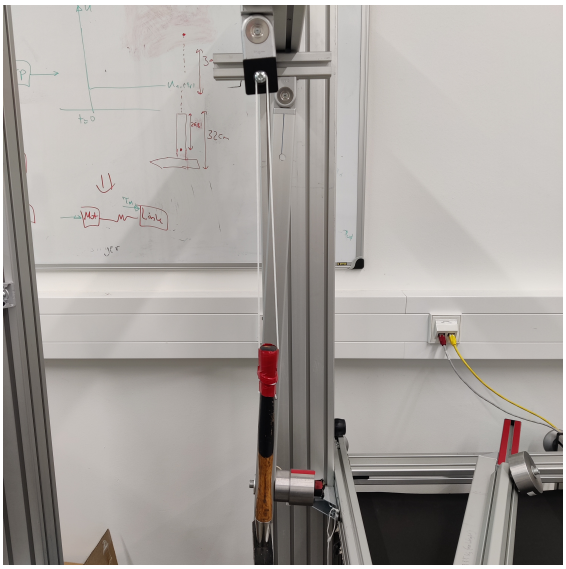

(a) Hammer experiment around *xx* axis.

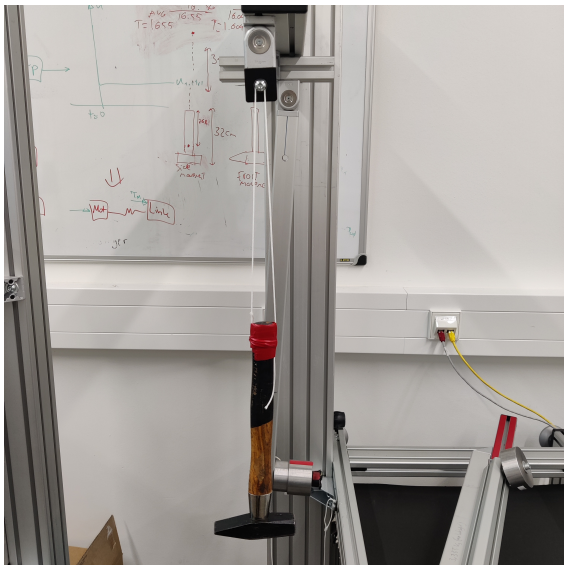

(b) Hammer experiment around *zz* axis.

Figure B.1: Hammer experiment setup

Appendix C

Hammer inertia

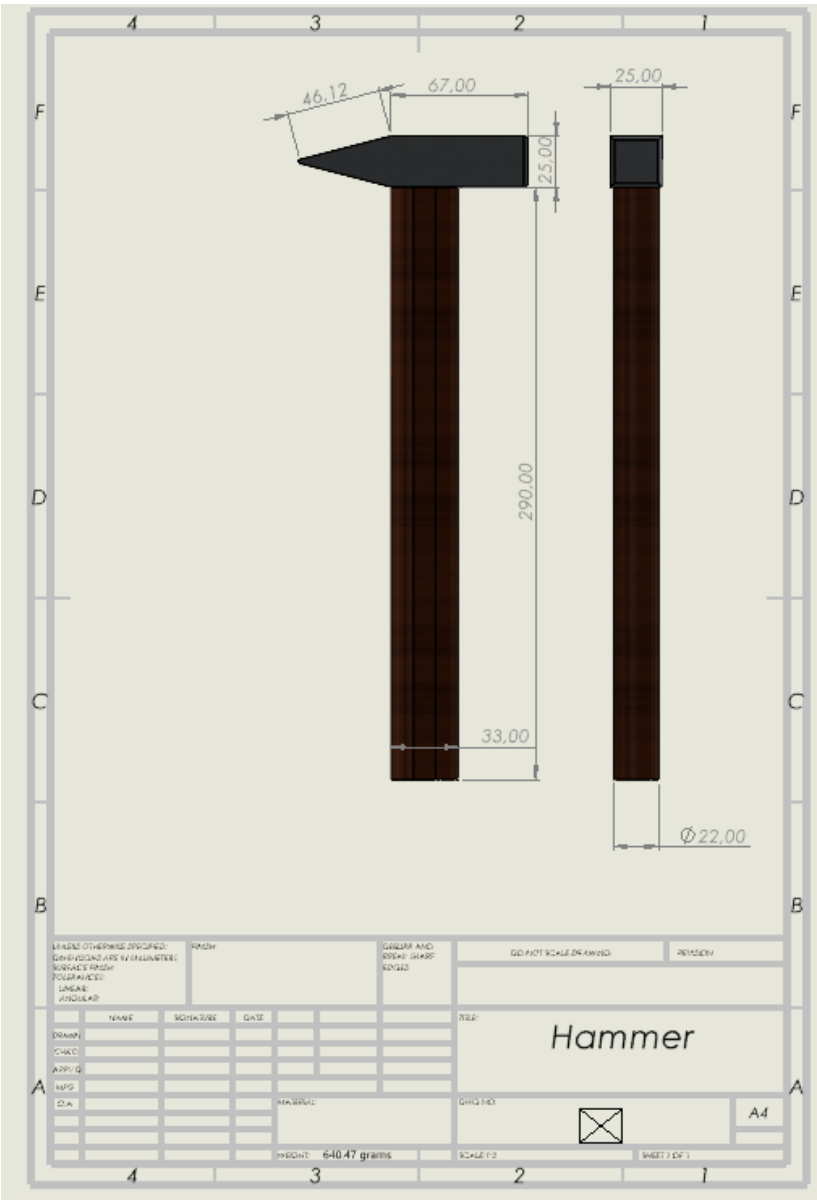

Figure C.1: Hammer in SolidWorks

Mass, center of mass and inertia matrix for the hammer and the links R5-UA, R6-AB, R7-FL combined.

$$m = 6.08842504\,\mathrm{kg} \tag{C.1}$$

$$\vec{r}_{cm} = \begin{bmatrix} 0.008176050263536 & 0.022672480514215 & 0.130512560415649 \end{bmatrix}^T \mathrm{m} \tag{C.2}$$

$$J_{cm} = \begin{bmatrix} 0.0974119951436790 & -0.0101443438265826 & -0.00627835869789591 \\ -0.0101443438265826 & 0.0725669377639631 & -0.0190140517507422 \\ -0.00627835869789591 & -0.0190140517507422 & 0.0447492435947301 \end{bmatrix} \mathrm{kg\,m^2} \tag{C.3}$$

Appendix D

Potential function comparison

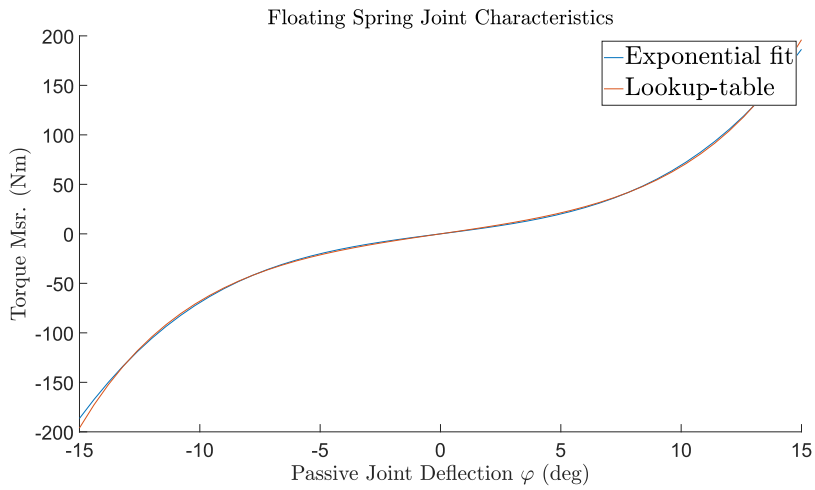

Figure D.1: Floating spring joint characteristics between lookup table and fitted polynomial function for $\sigma = 5.1°$

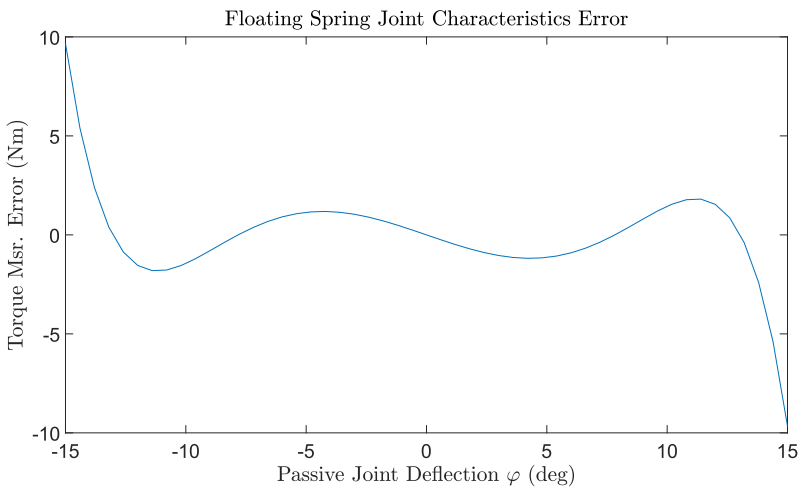

Figure D.2: The error between the lookup table and the fitted polynomial function of Figure D.2. The function was fitted between $12° < \varphi < 12°$, this can clearly been observed in the figure.

Appendix E

Nonlinear normal mode visualisation

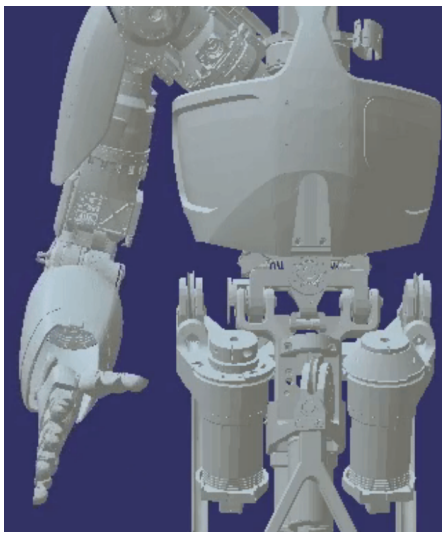

(a) Visualisation zero velocity at Generator 2.1

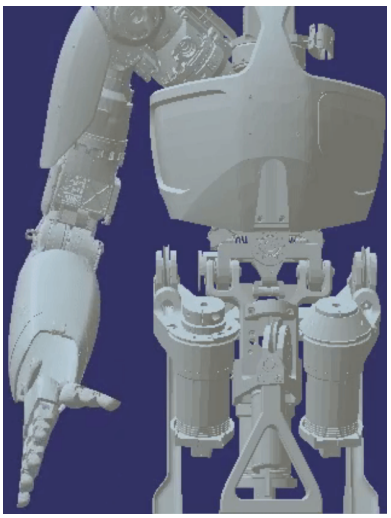

(b) Visualisation zero velocity at Generator 2.2

Figure E.1: Candidate 1: elbow driven hammering motion visualisation snapshots

(a) Visualisation zero velocity at Generator 3.1

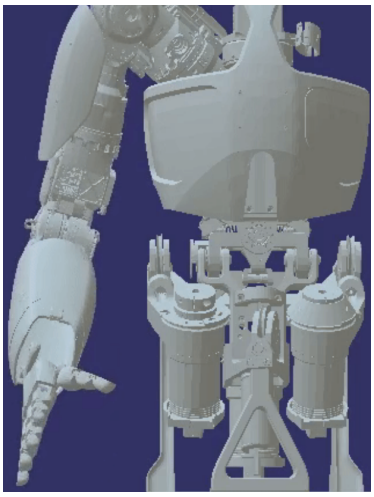

(b) Visualisation zero velocity at Generator 3.2

Figure E.2: Candidate 2: shoulder driven hammering motion visualisation snapshots

Appendix F

Effects link-side damping

The same simulation as in Chapter 3.3 but dependent on time. As shown in Figure F.1a, the link positions converge to the equilibrium position of $q_{eq} = \begin{bmatrix} -0.45 & 0.16 & 0.13 & 1.38 \end{bmatrix}$ rad. for positive damping (decreasing energy levels). In Figure F.1b the opposite is shown where the system is initialized close to the equilibrium position and the damping is negative. The corresponding energy levels can be seen in Figure F.2a and F.2b.

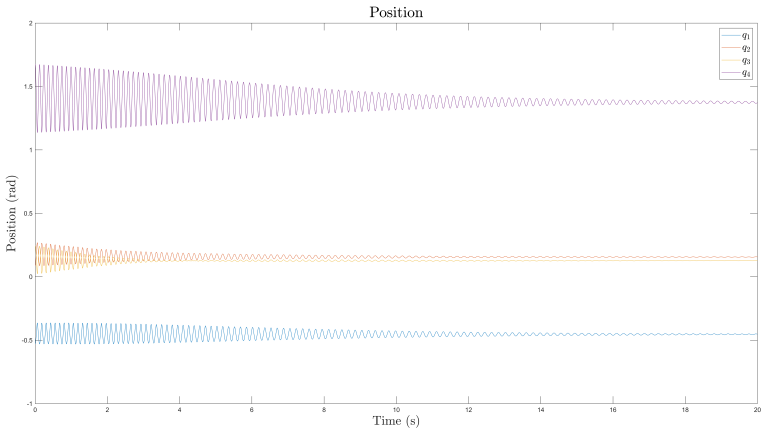

(a) Simulated modes over time for the energy dissipation case

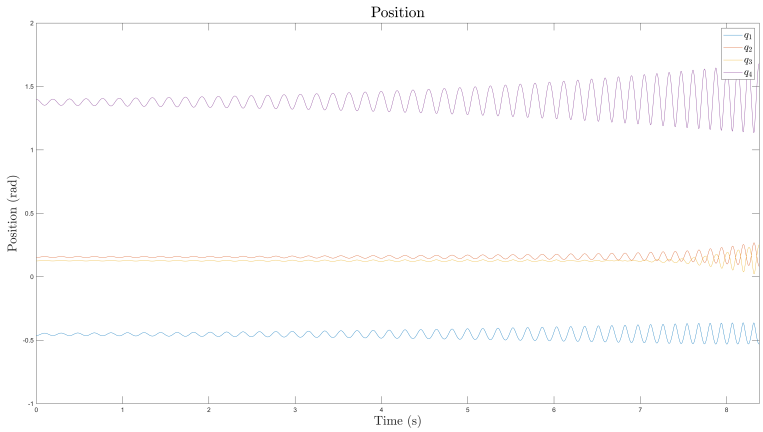

(b) Simulated modes over time for the energy injection case

Figure F.1: Effects of link-side damping on position

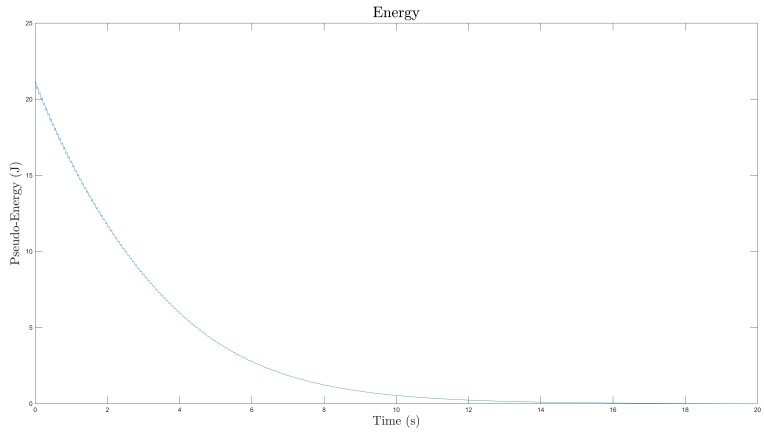

(a) Energy plot for the energy dissipation case, starting at 21 J and converging to 0 J

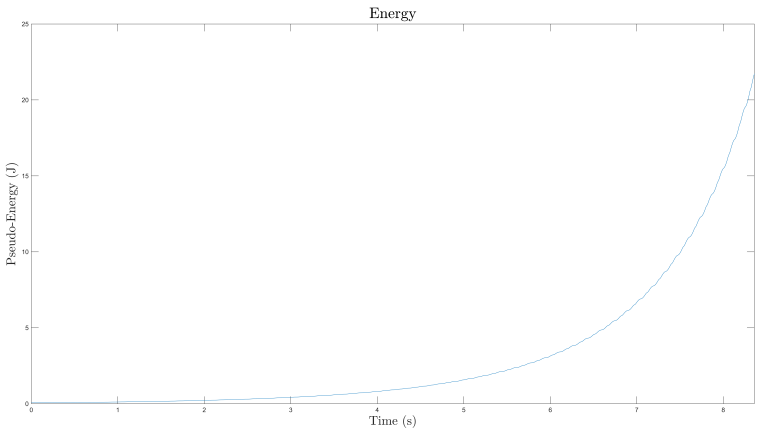

(b) Energy plot for the energy dissipation case, starting at 0.06 J and ending at 22 J

Figure F.2: Effects of link-side damping on energy levels